Preferential oxidation of CO in excess H_2 over CuO/CeO_2 catalysts: Characterization and performance as a function of the exposed face present in the CeO_2 support

D. Gamarra[a,1], A. López Cámara[a], M. Monte[a], S.B. Rasmussen[a], L.E. Chinchilla[b], A.B. Hungría[b], G. Munuera[c], N. Gyorffy[d], Z. Schay[d], V. Cortés Corberán[a], J.C. Conesa[a], A. Martínez-Arias[a,*]

[a] Instituto de Catálisis y Petroleoquímica, CSIC, Campus de Cantoblanco, C/Marie Curie 2, 28049 Madrid, Spain
[b] Universidad de Cádiz, Departamento de Ciencia de Materiales, Ingeniería Metalúrgica y Química Inorgánica, Facultad de Ciencias, 11510 Puerto Real, Cádiz, Spain
[c] Departamento de Química Inorgánica e Instituto de Ciencia de Materiales (Centro Mixto Universidad de Sevilla-CSIC), 41092 Sevilla, Spain
[d] Institute of Isotopes, Hungarian Academy of Sciences, H 1525-Budapest, Hungary

ABSTRACT

A series of oxidised copper-cerium nanostructured catalysts prepared by impregnation of copper over ceria supports synthesized by different methods (hydrothermal with varying preparation parameters, microemulsion/precipitation), in order to achieve different specific morphologies (nanocubes, nanorods and nanospheres), have been examined with respect to their catalytic properties for preferential oxidation of CO in excess H_2 (CO-PROX). The catalysts have been characterized in detail by XRD, Raman, S_{BET} measurement, HREM, XPS, TPR and EPR, which allows establishing a model of structural characteristics of the catalysts. The characterization results have been correlated with analysis of CO-PROX catalytic properties by means of catalytic activity measurements complemented by *operando*-DRIFTS. Structural dependence of the CO oxidation reaction on the dispersed copper oxide entities as a function of the exposed face present at the surface of the different ceria supports is revealed. An important overall enhancement of the CO-PROX performance is detected for the sample supported on ceria nanocubes which is proposed to be a consequence of the interaction between copper oxide and (1 0 0) faces of the ceria support.

© 2012 Elsevier B.V. All rights reserved.

1. Introduction

Hydrogen production from hydrocarbons for its use as fuel of proton exchange membrane fuel cells requires a final purification step in order to decrease the CO concentration resulting after reforming and water-gas shift (WGS) steps. Among different possible alternatives, preferential or selective catalytic oxidation of CO upon introduction of a small amount of O_2 in the H_2-rich stream (CO-PROX) is considered as most interesting from practical and economical points of view, most particularly for mobile applications [1]. Among different possible alternatives, catalysts combining copper and cerium oxides have demonstrated promising characteristics for CO-PROX, being able to compete with less economically interesting noble metal catalysts [1,2].

Main properties of $CuO-CeO_2$ systems for this process appear related to synergetic interactions between the two constituent oxides which determine interfacial characteristics [3]. This is based on the fact that active sites for the CO oxidation reaction, whose relative activity with respect to that of competing H_2 oxidation reaction basically determines overall performance for the process [4–6], are proposed to be located at such interface between both oxides [4,5,7,8], being formed by Cu^+ entities which result from ceria-promoted reduction of dispersed CuO upon interaction with the reactant mixture [4,5,9–14]. In turn, active sites for the H_2 oxidation reaction are apparently formed over the dispersed copper oxide particles upon extension of their reduction from the interface [5]. The fact that different active sites could be responsible for the two competing reactions is in agreement with kinetic measurements showing the absence of dependence of CO and H_2 oxidation rates with respect to H_2 and CO partial pressures, respectively, thus suggesting no important competency between the two reactants for the active sites [6,15]. However, it cannot be discarded that some degree of competency arises at high reaction temperature, in the non-selective region, when CO desorption from active reduced

* Corresponding author. Tel.: +34 915854940; fax: +34 915854760.
  E-mail address: amartinez@icp.csic.es (A. Martínez-Arias).
[1] Present address: Universidad de Extremadura, Campus de Badajoz, Avda. Elvas s/n. Edificio Guadiana, 06006 Badajoz, Spain.

copper sites becomes favoured, even though, to the best of our knowledge, no direct evidence for this is available yet [16]. Indeed, kinetic models are available in which such competency appears also reflected [17]; certainly, the origin of the discrepancy in macroscopic kinetic results can be related to the continuous changes in surface chemical characteristics upon interaction with the reactant mixture as a function of reaction temperature, nature of reactant mixture and type of sample examined [4,5,18,19]. Notwithstanding such controversy, there is general agreement that the mentioned copper oxide reduction process (related to an induction step taking place upon interaction of the catalyst with the reactant mixture [4,12]) leading to generation of active sites for the two reactions, as well as the catalytic activity over these sites, must in principle depend strongly on interfacial properties, which should be taken into account in order to explain observed ceria promoting effects [5,7,8,10,20].

In this respect, a possible way to tune interfacial interactions between the two oxide components could consist in changing the geometric type of interacting surfaces. In this sense, Skårman et al. reported a study on systems of copper oxide deposited on CeO_2 thin films prepared by rf magnetron sputtering showing the higher magnitude of synergetic effects between copper oxide and ceria (0 0 1) surfaces, compared to thermodynamically most stable (1 1 1) ones, for CO oxidation [21]. In a similar sense, Zhou et al. reported a higher CO oxidation activity of copper oxide dispersed on high-energy, more reactive (0 0 1) and (1 1 0) planes of CeO_2 nanorods prepared by a hydrothermal method in comparison with an analogous sample in which the ceria support was prepared by simple precipitation and which is assumed to expose mainly (1 1 1) surfaces [22]; in the same sense, NO reduction by CO was shown to be most favoured for CuO entities in contact with ceria nanorods compared with nanocubes or nanopolyhedra [23]. Concerning the CO-PROX application, only one very recent work following this type of approach seems to be available [24]. In contrast to the two mentioned works [21,22], in this latter report CO oxidation was found to be most favoured over copper oxide deposited on ceria nanooctahedra (exposing (1 1 1) faces), which in turn apparently displayed higher surface copper content according to XPS measurement than on ceria nanorods ((1 1 0) and (1 0 0) faces) or nanocubes ((1 0 0) faces) [24].

Considering these apparent discrepancies and in order to shed some more light in this respect, the present work analyses CO-PROX performance of catalysts of copper oxide (1 wt.% in all cases) deposited on different nanocrystalline ceria supports prepared by hydrothermal or microemulsion/precipitation methods, which display specific morphologies exposing different crystal planes of the CeO_2 lattice. For this purpose, a multitechnique approach (XRD, Raman spectroscopy, S_{BET}, HREM, XPS, EPR, TPR) has been followed for catalysts characterization while catalytic properties have been examined by conventional catalytic testing as well as *operando*-DRIFTS. The results show an important enhancement of CO-PROX characteristics for a sample supported on ceria nanocubes exposing (1 0 0) faces; this is attributed to the particular capability of such surface structure for a favourable interaction with active copper oxide entities which allows achieving for them a high dispersion degree (or, in other words, avoiding segregation of non-interacting entities).

2. Experimental

2.1. Sample preparation

Procedures available in the literature have been employed to prepare CeO_2 supports in the form of nanorods and nanocubes [25]. For this, $Ce(NO_3)_3 \cdot 6H_2O$ (Aldrich) used as the cerium precursor was dissolved along with NaOH in deionized water. Then, the mixture was introduced in Teflon flasks of 125 mL filled at 75% of the total volume and, after stirring, was held in a stainless steel autoclave and subjected to hydrothermal treatment during 24 h at 100 °C or 180 °C for the synthesis of ceria nanorods or nanocubes, respectively. After the hydrothermal treatment, the precipitates were separated by centrifugation, washed with deionized water and ethanol several times, followed by drying at 60 °C under air overnight. A third CeO_2 support (with final shape close to nanospheres, as will be shown below) was prepared by microemulsion method, using methods as reported elsewhere [26]. Briefly, cerium(III) nitrate was introduced in a reverse microemulsion (water in oil) using *n*-heptane as the organic phase, Triton X-100 (Aldrich) as surfactant, and hexanol as cosurfactant. Then, this suspension was mixed with another similar suspension containing as aqueous phase an alkali solution (TMAH, Aldrich) in order to precipitate the cerium. The resulting mixture was stirred for 24 h, centrifuged, decanted, and rinsed with methanol. Finally, the solid portion was dried overnight at 100 °C. Following drying, the three supports were calcined under air for 2 h at 500 °C. Basic physicochemical characteristics of these CeO_2 supports along with the nomenclature employed for them (where NC, NR and NS hold for nanocubes, nanorods and nanospheres, respectively, in accordance with shapes observed, see below) are summarized in Table 1.

Samples of copper supported on the three CeO_2 supports (Cu wt % of 1.0) were prepared by incipient wetness impregnation of the supports with copper nitrate aqueous solutions. Following impregnation, the samples were dried overnight at 100 °C and finally calcined under air at 500 °C for 2 h. Their characteristics are summarized as well in Table 1.

2.2. Techniques

Powder XRD patterns of the samples were recorded on a Seifert XRD 3000P diffractometer using nickel-filtered Cu K_α radiation operating at 40 kV and 40 mA, using a 0.02° step size and 2 s counting time per point. Analysis of the diffraction peaks was done with the computer program ANALYZE Rayflex Version 2.293.

Raman spectra were obtained at room temperature (RT) with a Bruker RFS-100 FT-Raman spectrometer provided with a diode-pumped germanium solid-state detector, which operates at liquid nitrogen temperature. A NdYAG laser (1064 nm) was used as excitation source at a power of 100 mW. Powdered samples were pressed in a holder and analyzed (100 scans, 4 cm^{-1} resolution) without further treatment. It must be noted that we have selected infrared excitation for these experiments because the use of visible excitation (results not shown) requires a careful control of exciting power (while keeping reasonable signal/noise ratio) in order to avoid a blue shift in the main triply degenerate F_{2g} mode of fluorite CeO_2 (only occurring for Cu-containing samples, results not shown) [27], which is likely a consequence of sample heating (and consequent lattice expansion) after electronic relaxation (considering that light absorption by Cu^{2+} entities extends to the visible region according to UV–vis analysis [28]); similar sample heating problems as a consequence of interaction with the visible Raman laser beam have been pointed out elsewhere [29,30].

High resolution electron microscopy (HREM) data, including high angle annular dark field (HAADF) images and X-ray energy dispersive spectra (XEDS), were recorded on a JEOL 2010 field emission gun transmission electron microscope operated at 200 kV equipped with an an EELS spectrometer GIF2000 (Gatan Imaging Filter) and an EDS spectrometer Oxford INCA Energy 2000 system. XEDS and EELS analysis were performed in STEM mode, with a probe size of ca. 1 nm and 0.5 nm, respectively. Specimens were prepared by depositing small portions of the samples to be investigated onto a molybdenum grid supporting a perforated carbon film. Deposition

Table 1
Specific surface area values, structural details extracted from analysis of the X-ray diffractograms and relevant parameters of the main fluorite F_{2g} Raman mode for the copper-ceria samples and corresponding reference ceria samples. CeO_2 crystallite size and microstrain values are based on analysis of the XRD peaks by means of Williamson-Hall linear fittings.

Sample	CeO_2 crystallite size (nm)	CeO_2 lattice parameter a (Å)	Microstrain ($\Delta d/d$)	F_{2g} frequency (cm^{-1})	F_{2g} FWHM (cm^{-1})	S_{BET} ($m^2 g^{-1}$)
CeO_2-NC	46	5.406	0.00012	463	15.5	20
CeO_2-NR	16	5.407	0.0021	463	24.0	76
CeO_2-NS	7	5.410	0.0019	462	23.3	130
Cu/CeO_2-NC	42	5.404	0.00020	463	15.5	14
Cu/CeO_2-NR	17	5.406	0.0019	462	25.9	75
Cu/CeO_2-NS	7	5.410	0.0025	460	28.2	115

was achieved by dipping the grid directly into the powder of the samples to avoid contact with any solvent.

X-ray photoelectron spectra (XPS) were recorded with a Leybold-Heraeus LHS10/20 spectrometer equipped with an EA-200 hemispherical electron multichannel analyzer (from Specs) and Al Kα X-ray source (1486.6 eV) operating at 11 kV and using a current of 30 mA. The samples, both supports and catalysts (0.2 mg), were slightly pressed into a small (4 mm × 4 mm) pellet and then mounted on the sample rod and introduced into the pretreatment chamber (volume ≈1 L) where they could be subjected to programmed thermal treatments (ramp of ca. 10 °C min^{-1}) up to 200 °C, then remaining at this temperature during 1 h under vacuum (ca. 10^{-8} Torr), under 5 Torr of pure reactive gases (e.g. CO or H_2) or under redox mixtures of reactive gases (e.g. CO/O_2 (2:1) or H_2/O_2/CO (6:3:1)) up to a total pressure of 10 Torr to mimic the catalysts surface states reached under equivalent catalytic conditions. Changes in the composition of the gas phase in the chamber during these treatments could be continuously monitored through a leak valve connected to a mass spectrometer (loss < 3%). Following each treatment, the sample was moved into the ion-pumped analysis chamber where it was further outgassed until a pressure lower than 2 × 10^{-9} Torr was attained (typically in about 1 h). This low pressure was maintained during all the data acquisition by ion pumping of the chamber. After each treatment, zones of the XP spectra in the relevant energy windows (in this order: Cu(2p), Cu($L_3M_{45}M_{45}$,^{1}G), Ce(3d), O(1s), C(1s) and a final wide scan spectrum 200–1450 eV) were collected at a pass energy of 44 eV which is typical of high resolution. The values of the Cu($2p_{3/2}$) and the Cu($L_3M_{45}M_{45}$,^{1}G) Auger line energies were used in the form of Wagner chemical-state plots to examine in detail the evolution of the copper state after such treatments. The intensities were estimated by calculating the integral of each peak after subtraction of Shirley-type background lines with the help of UNIFIT (version 2009) software; atomic ratios were then derived using the appropriate experimental sensitivity factors. All binding energies (BE) were referenced to the peak u‴ of Ce(3d) spectra characteristic of Ce^{4+} set at 917.0 eV. This reference gave BE values for all the recorded zones with an accuracy of ± 0.2 eV compared with the NIST database [31]. The presence of adventitious carbon, when it was present, was detected by a C(1s) line appearing at 285.0 ± 0.4 eV. Different pellets of the samples were submitted to similar sets of consecutive treatments (e.g. CO/O_2(2:1)–200 °C/1 h followed by CO/H_2/O_2(1:6:3)–200 °C/1 h, or CO–200 °C/1 h, followed by CO/O_2(2:1)–200 °C/1 h, etc.) which allow a comparative XPS analysis of the changes observed in the surface of each sample after the respective experiments.

For the EPR measurements, a Bruker EMX spectrometer with a 12 kW 10″ magnet was employed. Samples (0.050–0.100 g) were placed into a micro-reactor cell specially designed for high temperature EPR measurements using a Bruker ER 4114 HT cavity [32,33]. Check spectra were first recorded in situ at 350 °C in a flow of 50 mL min^{-1} under 10% O_2/He. After thermal equilibration and acquisition of a check high temperature spectrum at stationary conditions, the sample was cooled to room temperature in the oxygen

containing gas. Thereafter the catalyst sample was subjected to a mild vacuum, around 2 × 10^{-5} mbar, in order to remove weakly adsorbed oxygen. The sample was then cooled to 77 K in a liquid nitrogen finger dewar, and low temperature spectra were acquired using a standard Bruker ER4102ST cavity. The resonance frequency was around 9.41 GHz for the spectra acquired in liquid N_2. Modulation frequency and amplitude were 100 kHz and 4 G, respectively. Quantitative estimation of the amount of species present in the spectra was performed by double integration of the corresponding EPR spectra and comparison with a copper sulphate standard.

Temperature programmed reduction (TPR) was measured in a flow system using 1% H_2/Ar premixed gas with flow rate of 30 mL min^{-1}. A cold trap filled with liquid nitrogen was placed after the reactor to remove water. The system was equipped with a thermal conductivity detector. About 40 mg catalyst was placed into a quartz U-tube and calcined in 5% O_2/He at 500 °C for 1 h using 40 mL min^{-1} flow rate and 10 °C min^{-1} ramp. The sample was cooled to room temperature, purged with Ar and after switching to the reducing gas mixture it was heated to 500 °C using 10 °C min^{-1} ramp.

Operando-DRIFTS analysis was carried out using a Bruker Equinox 55 FTIR spectrometer fitted with an MCT detector. The DRIFTS cell (Harrick) was fitted with CaF$_2$ windows and a heating cartridge that allowed samples to be heated to 500 °C. Aliquots of *ca.* 100 mg were calcined in situ (in a similar way as employed for the catalytic tests, as shown below) and then cooled to room temperature under diluted oxygen before introducing the reaction mixture and heating in a stepped way, recording one spectrum (average of 50 scans at 4 cm^{-1} resolution) typically every 10 °C after the signals of different monitored gases (analysed on line by means of a quadrupole mass spectrometer Pfeiffer Omnistar) become constant (i.e. steady state conditions). The gas mixture (1% CO + 1.25% O_2 + 50% H_2 in He at 1 bar) was prepared using mass flow controllers in order to achieve conditions similar to those employed for the reaction tests with the tubular reactor described next.

The catalysts calcined in situ (under oxygen diluted in Ar at 500 °C) were tested in a glass tubular catalytic reactor for their activity under an atmospheric pressure flow (using mass flow controllers to prepare the reactant mixture) of 1% CO, 1.25% O_2 and 50% H_2 (Ar balance), at a rate of 500 cm^3 min^{-1} g^{-1} (roughly corresponding to 40,000 h^{-1} GHSV) and using a heating ramp of 5 °C min^{-1}. Analysis of the feed and outlet gas streams was done by gas infrared (Perkin-Elmer FTIR spectrometer model 1725X, coupled to a multiple reflection transmission cell – Infrared Analysis Inc. "long path gas minicell", 2.4 m path length, *ca.* 130 cm^3 internal volume-) while the m/e = 32 signal from the mass spectrometer was used to analyse the O_2 concentration. No products other than those resulting from CO or H_2 combustion (i.e. CO_2 and H_2O; note that possible contributions of WGS or reverse WGS must be residual under the conditions employed and, if at all, would take place only at temperatures higher than ca. 200 °C over this type of catalysts [34]) were detected in the course of the runs, in agreement with previous results on catalysts of this type [4,18]. On this basis,
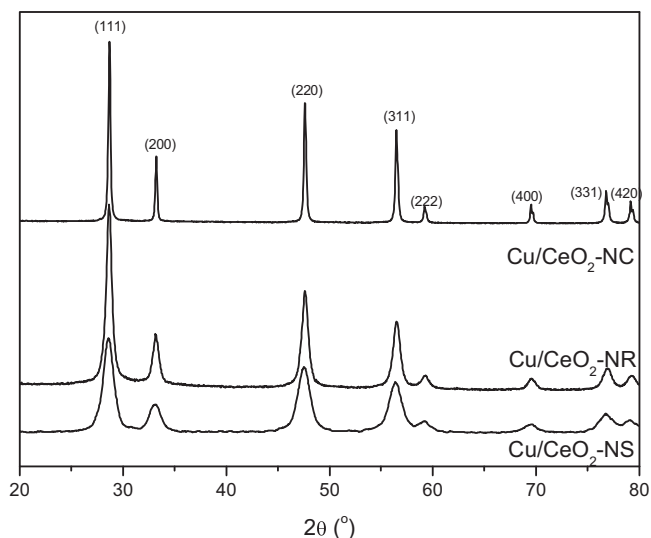
Fig. 1. X-ray diffraction patterns of the indicated samples. Miller indices for the fluorite diffractions are marked.

Fig. 2. Raman spectra of the indicated samples.

values of percentage conversion and selectivity in the CO-PROX process are defined as:

$$X_{CO} = \frac{F_{CO}^{in} - F_{CO}^{out}}{F_{CO}^{in}} \times 100, \quad S_{CO_2} = \frac{X_{CO}}{2.5 X_{O_2}} \times 100, \quad X_{O_2}$$

$$= \frac{F_{O_2}^{in} - F_{O_2}^{out}}{F_{O_2}^{in}} \times 100$$

where X and S are percentage conversion and selectivity, respectively, and F is the (inlet or outlet) molar flow of the indicated gas. Specific activity for the CO oxidation reaction was estimated from data at conversion percentage below $\approx 15\%$ in order to be under conditions as close as possible to kinetically meaningful differential ones.

3. Results and discussion

3.1. Characterization

Fig. 1 displays the X-ray diffractograms of the Cu-containing samples. Only diffraction peaks attributable to the fluorite phase of ceria are observed in all cases. Analysis of the peaks by means of Williamson-Hall (W-H) plots (not shown) reveals that the particle size remains close to that of the corresponding parent CeO_2 reference samples, in good qualitative agreement with specific surface area values observed for the samples (Table 1). As collected in Table 1, lattice parameters estimated from peak analysis are close to that expected for pure ceria for all the samples; a small decrease is generally noted with increasing crystal size as a consequence of size effects [35–38]. However, it must be noted that this does not discard that Ce-Cu mixed oxide (whose formation has been proposed to be favoured for the nanorod shape in samples of this type also prepared by impregnation [24]) may have been formed to some degree since practically no change in cell dimension was estimated from previous analyses when such substitutional copper incorporation occurs, as discussed in detail elsewhere [4,39–41]. In this sense, microstrain values estimated from the W-H plots for the Cu-containing samples (showing, as expected, a decrease with increasing crystal size [37,41]) are close to those for the corresponding parent CeO_2 samples, thus suggesting that no important copper incorporation to the fluorite lattice is produced in any case, as generally expected for samples prepared by impregnation and
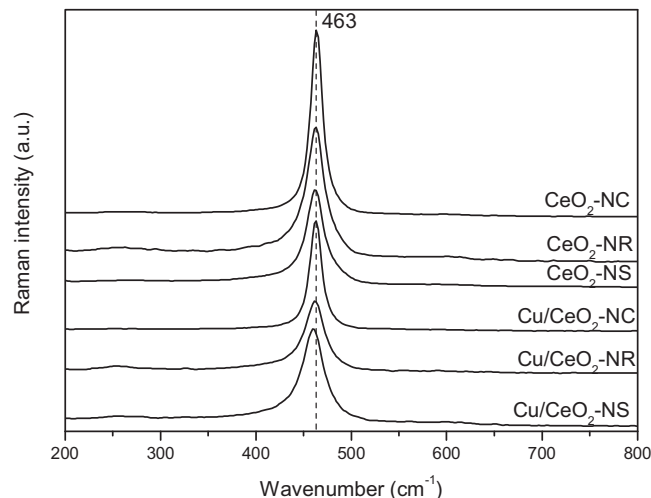
subjected to thermal treatment at relatively low temperatures [4]. It must be noted in this sense that, in contrast, important microstrain increase was previously detected upon copper incorporation to the fluorite CeO_2 lattice for samples prepared by coprecipitation of Cu and Ce within a microemulsion [4].

Further insight into the possibility that part of the copper might be incorporated into the CeO_2 fluorite lattice can be achieved by Raman spectroscopy, as shown elsewhere [4]. Thus, a main band at about 463 cm^{-1}, which corresponds to the triply degenerate F_{2g} mode of fluorite CeO_2 (the only one allowed in first order) is expected for pure CeO_2 [4,42,43]. Incorporation of Cu^{2+} in the fluorite CeO_2 lattice has been reported to produce the following effects. First, the appearance of a broad band extending between about 500 and 650 cm^{-1}, which has been related to the presence of oxygen vacancies [44], as a consequence of substitutional incorporation of Cu^{2+} into the fluorite lattice which must be accompanied by generation of oxygen vacancies for charge balance ($Ce^{4+} + O^{2-} \leftrightarrow Cu^{2+} + V_{\ddot{O}}$; being $V_{\ddot{O}}$ a doubly ionized oxygen vacancy). However, observation of such broad band can be difficult for relatively low oxygen vacancies concentration. In this sense, most sensitive evidence of copper incorporation in the lattice can be provided by the blue shift and increase in width observed by Raman for the main F_{2g} mode band [4]. This has been related to influence of phonon confinement and possibly inhomogeneous strain in the presence of oxygen vacancies in the fluorite lattice [4,38,43]. Fig. 2 displays the Raman spectra of the samples. Only subtle differences are detected in mentioned parameters as a function of the presence of copper in the catalysts, as collected in Table 1. Thus, relatively small differences are observed for –NC and –NR samples while somewhat higher change is observed for –NS samples. On this basis and comparing with previous results on microemulsion/coprecipitated samples in which copper incorporation to the fluorite lattice was demonstrated by different techniques [4], incorporation of copper, if at all, must be residual in Cu/CeO_2-NC or Cu/CeO_2-NR while it could affect to a stronger extent to Cu/CeO_2-NS sample. This latter is supported by incipient presence of a weak broad band at ca. 600 cm^{-1} for this sample, according to arguments exposed above.

Wide scan XP-spectra (100–1450 eV) of the three CeO_2 supports outgassed at 150 °C during 2 h in the preparation chamber (hereafter referred to as original samples) show only the presence of cerium, oxygen and carbon in all the spectra. Thus, Ce(3d), O(1s) and C(1s) zone spectra were recorded in further detail. Analysis of these spectra gives O/Ce atomic ratios of 2.35, 2.23 and 1.93 for the CeO_2-NC, CeO_2-NS and CeO_2-NR supports, respectively. In all

cases the Ce(3d) spectra show that the CeO_2 original surfaces are fully oxidized (i.e. Ce^{4+}) while in the C(1s) zone ($E_B \approx 300$–$280\,eV$) a small shoulder at ca. 285.3 eV, due to some carbonaceous contamination (<1%), is overlapped to a more intense Ce(4s) peak at 289.7 eV (where also carbonate species, if present, would appear). Differences between the three supports are detected in the O(1s) spectra. Thus, a well defined and symmetric main peak at 529.5 eV along with an overlapping weaker one at ca. 531.8 eV exists in CeO_2-NC in contrast with a broad asymmetrical O(1s) peak observed for the other two supports.

XPS calculated chemical composition for the Cu/CeO_2 catalysts, expressed as Cu/(Cu + Ce) atomic ratios, yields values of 16.5, 11.5 and 11.8 for Cu/CeO_2-NC, Cu/CeO_2-NR and Cu/CeO_2-NS, respectively. Taking BET specific surface areas in Table 1, it can be estimated that the concentration of Cu (as CuO) at the surface of Cu/CeO_2-NS would be of the order of $\sim 7.3 \times 10^{13}$ Cu/cm^{-2}, a value close to one monolayer of CuO spread on the CeO_2 in this sample. Then the same amount of copper would produce 1.7 and 6.5 theoretical CuO monolayers for Cu/CeO_2-NR and Cu/CeO_2-NC respectively (thickness of a monolayer ca. 2.38 Å by assuming an average $d_{111}(CuO)/d_{111}(Cu_2O)$ value). However, XPS chemical composition data suggest that for Cu/CeO_2-NC most of the copper oxide must be in the form of discrete particles with a thickness much higher than ~ 15 Å ($3\lambda_{Cu(2p)} \approx 3 \times 5.0$ Å, where $\lambda_{Cu(2p)}$ is the inelastic mean free path of the Cu(2p) photoemission in the copper oxide layer), so that a fraction of the copper is not being detected in this sample. In turn, the presence of such relatively thick copper oxide particles would contribute to a higher Cu/(Ce + Cu) ratio with respect to the other two samples as a consequence of a slight shadowing of the Ce(3d) signal, similar to observations by Skårman et al. on samples of copper oxide films on ceria [21].

To complement the structural analysis, the catalysts were examined by HREM. Representative images of the CeO_2 supports are shown in Fig. 3. This evidences the different morphologies obtained as a function of differences in the preparation parameters and in agreement with previous investigations [25,45]. Thus, nanocubes, nanorods and nanospheres (or nanopolyhedra) shapes are observed, which basically expose (1 0 0) faces for CeO_2-NC and (1 0 0) and (1 1 0) faces for CeO_2-NR, while CeO_2-NS crystals basically show a shape close to nanospheres with polyhedral shape, most likely exposing diverse faces in which the thermodynamically most stable (1 1 1) face can apparently predominate.

Many HREM and STEM-HAADF micrographs along with XEDS and EELS spectra have been recorded in order to characterize the Cu-containing catalysts. The HREM images generally show the presence of aggregates of multiple nanoparticles displaying lattice fringes whose interplanar distances and angles are compatible with the presence of the fluorite ceria phase in all cases. In general, the same faces as those observed for the Cu-free supports appear exposed at the surface of the ceria crystals in the Cu-containing catalysts. No copper-containing phase could however be resolved in any of the multiple HREM images taken for these samples. STEM-HAADF images of Cu/CeO_2-NC and Cu/CeO_2-NR basically confirm the sample morphologies detected in direct images and, since their intensity depends primarily on the atomic number and sample thickness, it could in principle be used to locate the copper entities. In this sense, HAADF-STEM images of Cu/CeO_2-NC and Cu/CeO_2-NR samples sporadically exhibit segregated particles with a different shape than expected for pure nanocubes and nanorods, respectively, and which could in principle correspond to copper-containing phases or to a residual fraction of CeO_2 nanoparticles with morphology different to the predominant nanocube or nanorod. In order to determine if these entities correspond to copper-containing phases, analytical techniques (XEDS and EELS) were used. All XEDS spectra acquired at any point of the Cu/CeO_2-NC, Cu/CeO_2-NR and Cu/CeO_2-NS samples displayed small peaks

corresponding to copper; however, their intensity was in no case higher than that detected when a pure ceria sample was studied as a reference. Considering that XEDS experiments were designed to avoid copper contamination by using a beryllium holder and molybdenum grids, observation of such small copper signal must be related to a contamination in the microscope column or accessories. Concerning analysis by EELS, all the analyzed spectra showed M_4 and M_5 lines of cerium but no evidence of copper could be resolved. The absence of copper detection in HREM images or by using XEDS or EELS analytical techniques on multiple pictures of the samples evidences that copper must be relatively well-dispersed in any of the samples. Selected examples of the electron microscopy characterization performed are presented in Fig. 4. Fig. 4a displays a HAADF-STEM image of Cu/CeO2-NC together with the EEL spectra acquired in positions 1 and 2, which are similar to the EELS of the CeO_2 reference while a sharp increase at the position typical of CuO is not seen. Fig. 4b displays a HAADF-STEM image of Cu/CeO2-NR which shows the rod shape and evidences the presence of pores (darker patches which means less thickness). The XEDS displayed as an example shows the mentioned residual copper signal coming from the microscope contamination. Fig. 4c presents a HREM image of Cu/CeO_2-NS in which the nanoparticles with irregular more or less spherical shape can be clearly seen. The digital diffraction pattern of the particle marked with an arrow shows interplanar spacing and angles typical of the ceria fluorite structure.

EPR spectra obtained at 77 K for the Cu-containing samples after pretreatment under diluted oxygen at 350 °C are displayed in Fig. 5. They are constituted by the overlapping of different signals, as exposed next. Two narrow axial signals with practically the same $g_\perp$ value at 1.967–1.966 and $g_{||} = 1.949$–1.948 and 1.944–1.941, respectively, are detected for the two hydrothermally prepared samples (Cu/CeO_2-NC and -–NR). These were earlier detected in CeO_2 samples and attributed then to Ce^{3+} ions associated to an anion vacancy (and thus in a very asymmetric environment which could quench to some extent the spin relaxation) or other times to electrons 'quasi-free' or trapped at anion vacancies, perhaps partially delocalized onto Ce ion orbitals [46,47]; however, more recent work suggests that they could correspond to Cr^{3+} impurities [48], which could originate from some of the precursors or from laboratory material employed during hydrothermal preparation. It must be noted that quantitative analysis indicates that they represent a very small concentration in any of the samples, corresponding to sub-ppm level in any case. On the other hand, different signals attributable to paramagnetic Cu^{2+} entities are also detected. Thus, a major featureless broad signal showing extremes at $g \approx 2.20$ and $g \approx 2.04$, signal B (following the nomenclature adopted in previous reports [9,49]), and two other superimposed minor axial signals in which four-line hyperfine splittings can be resolved in each of its components (signal C1 at $g_{||} = 2.233$, $A_{||} = 16.0 \times 10^{-3}\,cm^{-1}$, $g_\perp = 2.036$ and $A_\perp = 1.8 \times 10^{-3}\,cm^{-1}$, and less intense signal C2 at $g_{||} = 2.274$, $A_{||} = 17.4 \times 10^{-3}\,cm^{-1}$, $g_\perp = 2.041$ and $A_\perp = 2.3 \times 10^{-3}\,cm^{-1}$ [9,49]) are observed in Cu/CeO_2-NR.

According to previous analysis [9,49], in which details can be found, signals C1 and C2 are typical of isolated Cu^{2+} ions in, to a first approximation, tetragonally expanded octahedral environments with the unpaired electron essentially residing in the d_{x2-y2} orbital, and with a relatively higher ligand bond covalency and ligand field for signal C1 while the magnitude of the tetragonal distortion appears fairly similar in both signals. In turn, signal B, showing an average <g> value close to those of type C signals, must also be due to Cu^{2+} ions; its larger line width (leading to unresolved hyperfine splitting) can be attributed to dipolar broadening effects caused by mutual interactions with neighbouring paramagnetic Cu^{2+} ions, indicating that the corresponding ions are located in a Cu^{2+}-containing aggregate phase of oxidic type. In this sense, taking into account that antiferromagnetic couplings between Cu^{2+} ions
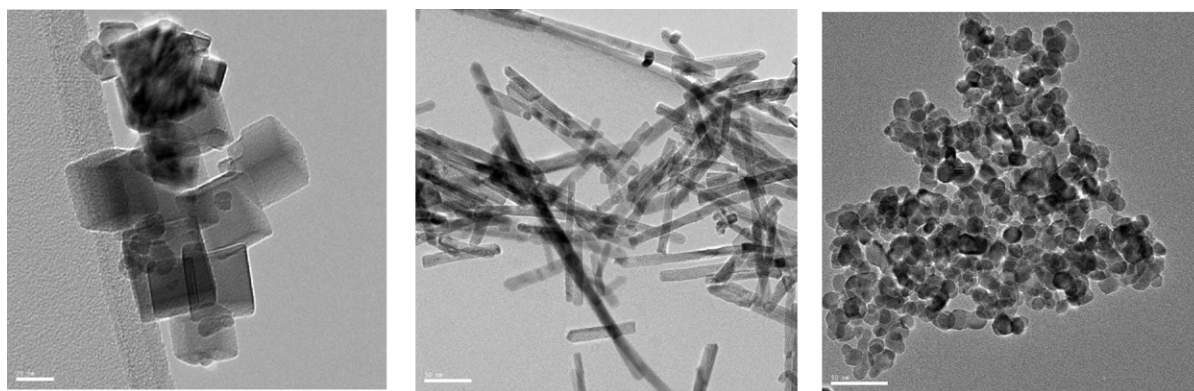
Fig. 3. TEM images of the different CeO_2 supports: CeO_2-NC (left), CeO_2-NR (middle) and CeO_2-NS (right). The horizontal scale bar shown corresponds to 50 nm except for CeO_2-NC for which it represents 20 nm.

in well-crystallized CuO phases produce EPR-silent species [50], Cu^{2+} ions yielding signal B can be considered as belonging to small copper oxide clusters where this antiferromagnetic character is not fully developed [9,49]. On the other hand, the spectrum of Cu/CeO_2-NS is constituted by the overlapping of a major signal B and minor signal C1 (with a residual amount of signal C2, according to perusal of perpendicular component zone) along with a new signal K characterized by an intense doublet centered at $g \approx 2.040$ in which the two components, separated by ca. 670 G, show a seven-line hyperfine splitting. This doublet corresponds to the perpendicular component of the signal of Cu^{2+} ion pairs formed by two equivalent ions of nearly axial symmetry [51,52]. This signal appears very well resolved (relatively sharp features for the hyperfine splitting of the parallel component are evident between ca. 2200 and 2800 G while sharp lines in the range 1400–1750 Gauss resulting from "forbidden" $\Delta M_s = 2$ transitions, also characteristic for such dimer species, were also observed, range not shown), which allows determining fully its parameters as $g_{\perp} = 2.040$, $g_{||} = 2.208$, $A_{\perp} = 1.35 \times 10^{-3}$ cm^{-1}, $A_{||} = 8.8 \times 10^{-3}$ cm^{-1}, and $D = 0.066$ cm^{-1}, D being the fine structure parameter. In contrast, Cu/CeO_2-NC shows only a very weak contribution of signals type C evidenced by weak sharp features in the corresponding perpendicular zone; signals B and K cannot be discerned. However, as a difference with the other two samples, the spectrum appears overlapped on a very broad signal with extremes occurring at about 1000 and 6000 G (range not shown). Such broad signal must correspond to Cu^{2+} ions affected by very strong dipolar or ferromagnetic coupling interactions [52] and suggests a different nature for the condensed copper oxide phase in this sample.

On the other hand, quantitative estimation of the amount of spins detected shows that about 24% of the whole copper present in the samples is detected in the spectra of Cu/CeO_2-NR or Cu/CeO_2-NS. Since a high temperature pretreatment under O_2 is known to generate fully oxidised CuO in this type of samples [3,4,10,12,64], the portion of copper which remains undetected must be attributed to relatively large CuO particles taking into account that, as mentioned above, antiferromagnetic couplings between Cu^{2+} ions in well-crystallized CuO phases produce EPR-silent species [50]. The overlapping wide signal present in Cu/CeO_2-NC disallows reliable quantitative estimation in this sense, although in any case the observed contribution of signals type C in this sample must constitute a residual amount of the whole copper present in the sample.

TPR profiles for the catalysts are displayed in Fig. 6. Two well separated reduction peaks are observed for Cu/CeO_2-NR and Cu/CeO_2-NS in contrast with Cu/CeO_2-NC which displays a single asymmetric peak. Deconvolution of the profiles by using Gaussian functions suggests however a more complex situation (Fig. 6 and Table 2). Thus, Cu/CeO_2-NR in which the two peaks appear more separated requires a third contribution for satisfactory

Table 2
Reduction temperatures (in °C) and relative intensities (in percentage of total area, between parentheses) of the peaks obtained upon deconvolution of TPR profiles for the indicated samples.

Cu/CeO_2-NC	Cu/CeO_2-NR	Cu/CeO_2-NS
195 (20)	185 (14)	190 (5)
223 (62)	205 (20)	220 (23)
245 (18)	246 (66)	252 (60)
		266 (12)

fitting. Multicomponent deconvolution is also required for achieving satisfactory fittings for the other two samples. The mentioned two peaks profile is typical for this type of samples [53–55]. It has been interpreted in two different senses. On the one hand, it was proposed to be related to reduction of two different types of copper oxide entities differing in their degree of interaction with the support [53]. The low temperature peak would correspond to smaller copper oxide particles subjected to a stronger interaction with the support which would favour their reduction while the high temperature peak would correspond to larger copper oxide particles [53]. This is mainly based on the fact that in ceria-supported copper samples the proportion of the high temperature peak with respect to the low temperature one increases with increasing the copper loading which is known to lead to segregation of large copper oxide particles [53]. An alternative interpretation for the two peaks profile was however put forward by Caputo et al. mainly on the basis of quantitative analysis of the profiles [55]. They observed, in agreement with other quantitative measurements [54,56–58], that the overall amount of hydrogen consumed during the TPR test up to 500 °C was higher than that required for full copper oxide reduction and thus that surface ceria reduction must be also contributing to the observed two peaks. Furthermore, the intensity of the high temperature peak appeared close to the portion required for support reduction, thus proposing that the high temperature peak was mainly related to that process, which overlaps in most cases with the reduction peak of large segregated copper oxide particles for samples with relatively high copper loading [55].

In any case, it is assumed, in agreement with results obtained by other techniques [59], that copper oxide becomes reduced in a single step ($Cu^{2+} \rightarrow Cu^0$) since sequential reduction ($Cu^{2+} \rightarrow Cu^+ \rightarrow Cu^0$) could not be resolved in any case. Results obtained here are in agreement with the Caputo et al. interpretation of sequential component reduction. Thus, the overall amount of hydrogen consumed is considerably higher than that required for full CuO reduction (157 μmol g^{-1}) in Cu/CeO_2-NR (453 μmol g^{-1}) and Cu/CeO_2-NS (422 μmol g^{-1}). This contrasts with 203 μmol g^{-1} used for reduction of Cu/CeO_2-NC. Furthermore, the main contribution to the high temperature peak in Cu/CeO_2-NR or Cu/CeO_2-NS
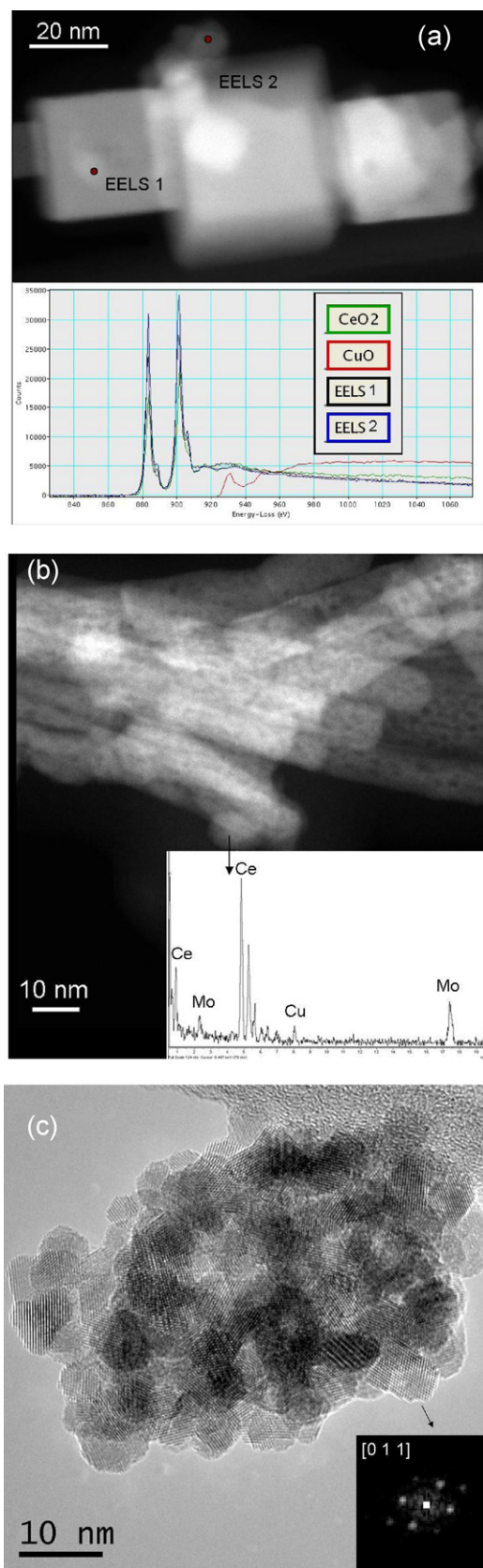
Fig. 4. (a) HAADF-STEM image of Cu/CeO_2–NC along with the EELS acquired in positions 1 and 2 as well as EELS of CeO_2 and CuO reference samples. (b) HAADF-STEM image of Cu/CeO_2-NR along with a representative XEDS spectrum. (c) HREM image of Cu/CeO_2-NS; the inset digital diffraction pattern, taken from the nanocrystal appearing near the lower right corner, shows ceria fluorite structure seen in the [0 1 1] direction.
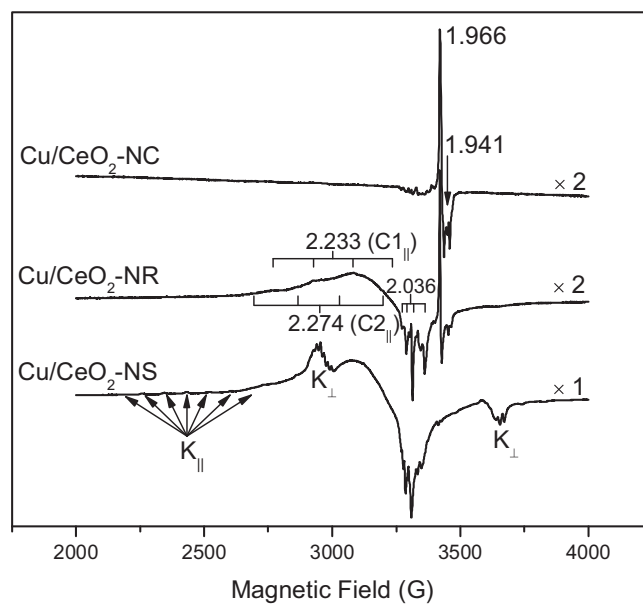
Fig. 5. EPR spectra at 77 K of the indicated samples after pretreatment under diluted oxygen at 350 °C and extensive outgassing at room temperature. Note only those features of signals mentioned in main text which appear most prominent and non-overlapping are labelled.
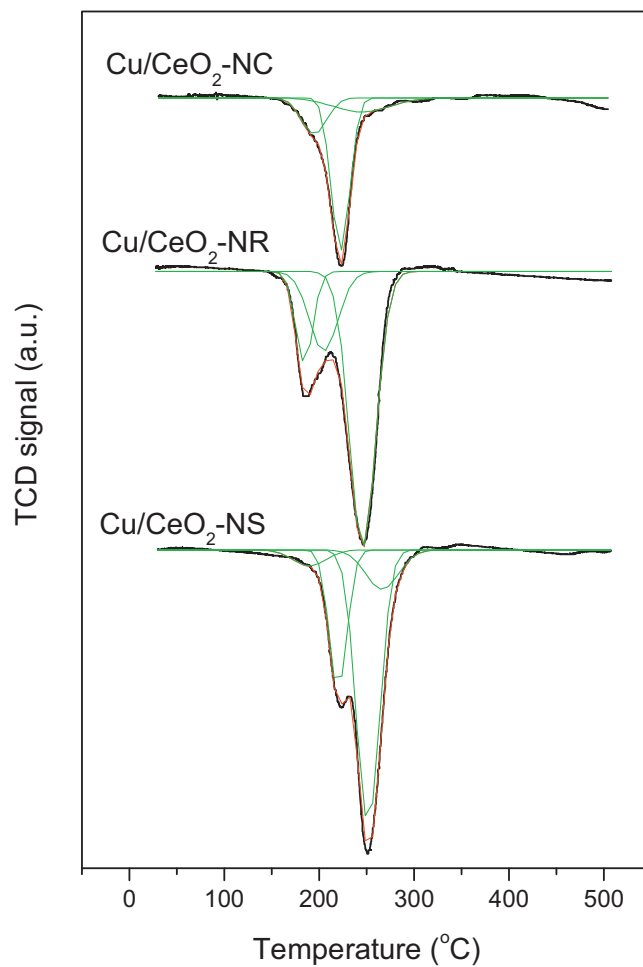
Fig. 6. TPR profiles obtained for the indicated catalysts. Deconvolution of the corresponding profiles is shown.

(at 246 and 252 °C, respectively) constitutes 66 and 60% of the whole H_2 consumption (Table 2), quite close to the 65 and 63% values which would correspond to support reduction according to quantitative estimation, respectively. For Cu/CeO_2-NC, a high temperature peak at 245 °C is required for satisfactory fitting of the profile. This latter constitutes 18% of the whole H_2 consumption (Table 2), close to the quantitative estimation of the amount of H_2 used for support reduction in this sample (23%), being therefore attributed to that process. Note that we are assuming in any case, as previously mentioned, that pretreatment under diluted oxygen at 500 °C leads to fully oxidised CuO as starting state, in agreement with previous investigation [3,4,10,12,64]. On the other hand, the amount of support which becomes reduced is in principle a function of the specific surface area (Table 1); discrepancy between Cu/CeO_2-NR and Cu/CeO_2-NS in this sense may well reflect the higher reducibility of the (1 1 0) face of ceria with respect to the (1 1 1) one, according to theoretical work [60–62]. In addition to mentioned peaks attributable to support reduction, TPR results support, in agreement with EPR ones, certain heterogeneity in copper oxide entities present in the catalysts on the basis of the presence of two low temperature reduction peaks for the three samples (Table 2). A third type of oxidised copper entity appears in Cu/CeO_2-NS yielding a high temperature peak at 266 °C. This may well correspond, in agreement with discussion above on Raman results, to the reduction of Cu^{2+} cations incorporated to the ceria fluorite lattice, proposed to be most difficult to reduce [4,39,40].

On the basis of the characterization results obtained, a structural model for the catalysts can be established, as shown in Fig. 7. Ceria is assumed in any case to favour a large dispersion of copper oxide entities on it. These would however differ in terms of respective thickness (even though keeping amorphous structures in any case; in this sense, a recent environmental TEM analysis was able to infer the presence of copper-containing amorphous entities over the ceria support upon redox treatment in samples of this type [59]) and/or degree of interaction with the underlying CeO_2 support. In this respect, comparison with previous work suggests that the ceria nanocube configuration with (1 0 0) exposed faces could exert a stronger interaction on copper oxide particles than the other examined configurations, which would favour a relatively higher dispersion for them; this is based on the fact that big segregated CuO particles were detected by XRD or HREM when the copper oxide loading is quintuplicated in a sample supported on CeO_2-NS [4] (while theoretical surface loading would still be lower than for Cu/CeO_2-NC, taking respective specific surface areas into account). Even though XRD, regardless of dispersion degree, could present limitations for detection of CuO for 1 wt.% copper loading samples, it must be noted that no such segregated big CuO particles could be observed upon exhaustive analysis of Cu/CeO_2-NC by HREM, as exposed above. It must be considered in this sense that most intense CeO_2 XRD peak is inferred to be about 7 times more intense than that of tenorite CuO for equimolar amount of Ce and Cu, according to previous work [63]; thus, taking the XRD pattern obtained for the mentioned 5 wt.% Cu sample supported on CeO_2-NS as a reference [4], i.e. assuming a similar CuO segregation would be produced for Cu/CeO_2-NC, the amplitude for most intense CuO peaks would have the same order of magnitude as the noise level under employed experimental conditions. The presence of relatively thick dispersed CuO particles in Cu/CeO_2-NC is in any case supported by XPS chemical composition data, as discussed above. In turn, certain heterogeneity in the dispersed CuO entities is inferred from EPR and TPR results suggesting the presence of a small amount of smaller (more reducible) CuO particles in Cu/CeO_2-NC as well as relatively big CuO crystals (even though not big enough to be detected by XRD) accounting for the portion of copper which remains undetected by EPR, according to discussion above. Heterogeneity in the type of copper oxide entities for

samples of this type prepared by impregnation, as those in this work, is in line with previous Ar^+-sputtering XPS analysis [10].

3.2. Catalytic properties

Fig. 8 shows catalytic activity results obtained for the three Cu-containing samples. As typically observed for this type of process [1,4], CO conversion evolution with increasing temperature shows first an increase up to a certain maximum value as a consequence of prevalence of the CO oxidation reaction and a final decrease when the H_2 oxidation reaction prevails, as reflected in CO_2 selectivity profiles too. Relatively small CO conversion differences are observed between Cu/CeO_2-NR and Cu/CeO_2-NS at low temperature; differences between them appear somewhat stronger with respect to H_2 oxidation activity, which is reflected by the differences observed in CO_2 selectivity profiles. These latter, as shown some years ago [64], display an irregular evolution at low reaction temperature for some of the samples which has been related to CO acting as gaseous promoter of low temperature residual H_2 oxidation activity [64]. In contrast to the behaviour observed for Cu/CeO_2-NR and Cu/CeO_2-NS, Cu/CeO_2-NC shows much poorer CO oxidation and H_2 oxidation activities. Nevertheless, due to the balance of activities between both oxidation reactions, this latter sample shows most efficient CO-PROX performance in the sense that the width of the window of CO conversion above 99% (outlet CO below 100 ppm) extends to about 90 °C in contrast to about 60 °C for Cu/CeO_2-NR or Cu/CeO_2-NS, which is reflected in the apparently higher CO_2 selectivity generally observed for Cu/CeO_2-NC. In turn, Arrhenius plots for the CO oxidation reaction elaborated with specific activity values extracted from the CO conversion profiles are displayed in Fig. 9. Apparent activation energy values determined from these plots exhibit appreciable differences between the catalysts while they are within ranges observed for that reaction over this type of catalysts in other reports [6,65,66].

On the other hand, since correlation in relative terms is found in some cases between CO and H_2 oxidation activities, an additional catalytic activity experiment was performed in which CO conversion levels of Cu/CeO_2-NR and Cu/CeO_2-NC were practically matched in a certain temperature range (upon increasing spatial velocity for the former with respect to the test shown in Fig. 8), in order to compare their CO_2 selectivity properties at the same temperature and CO conversion. The better CO_2 selectivity provided by Cu/CeO_2-NC is confirmed by this experiment as illustrated in Fig. 10 . As expected over this type of catalysts [67], a general increase in CO_2 selectivity is observed upon increasing spatial velocity for Cu/CeO_2-NR; in spite of this, Cu/CeO_2-NC presents apparently higher CO_2 selectivity in most of the examined range, particularly when practical high CO conversion levels are attained.

3.2.1. XPS study of the reactivity of samples

In order to attempt to rationalize catalytic results above, the effects of reaction under CO on the catalysts (and their supports) were examined by XPS (as well as by *operando*-DRIFTS, below). Similar sets of XPS experiments were carried out with the catalysts and corresponding supports using pure CO, and CO/O_2 or $CO/H_2/O_2$ mixtures up to 200 °C (see Experimental) to examine the state of their surfaces after each experiment. After reduction with CO at 200 °C for 1 h the two O(1s) peaks of the CeO_2-NC support are sharper and better resolved while a very small signal due to CO_2 (m/e = 44) and traces of H_2O (m/e = 18) are detected when monitoring the gas phase during the experiment. Surface reduction was confirmed by the presence in the Ce(3d) spectra of traces of the two main peaks (at 885.9 and 904.4 eV) of Ce($3d_{5/2}$) and Ce($3d_{3/2}$) states of Ce^{3+}, respectively, and by the change of the O/Ce atomic ratio from 2.35 to 2.13 at the end of the experiment. Meanwhile, a small C(1s) broad signal at ca. 285.8 eV indicates a small deposition
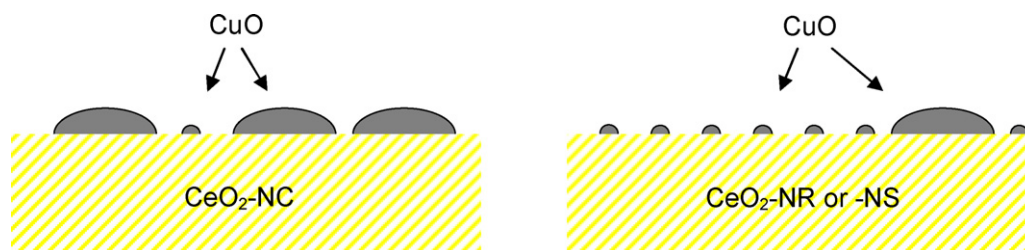
Fig. 7. Schematic structural model proposed for the Cu-containing catalysts on the basis of characterization results (see main text for details).

of some carbonaceous species; in this sense, CO disproportionation upon CO interaction with reduced ceria was recently detected by Wu et al. [45]. However, interaction of this slightly reduced CeO_2-NC pellet with stoichiometric $CO + O_2$ mixture at 200 °C restores the original oxidized clean surface (giving now O/Ce = 2.08), while mass monitoring of the gas phase indicates a slow oxidation of CO reaching ca. 30% conversion of the original $CO + O_2$ mixture at the end of the experiment. Treatment under CO-PROX conditions (using $CO:H_2:O_2 = 1:6:3$ at 200 °C for 1 h) leads to similar results, showing a CO_2 selectivity >99%, while the two O(1s) peaks appear now much broader (similar to those in the original CeO_2-NR and CeO_2-NS supports), and the O/Ce atomic ratio increases up to 2.50. Subtraction of the O(1s) spectra, Fig. 11, shows the existence of a third type of
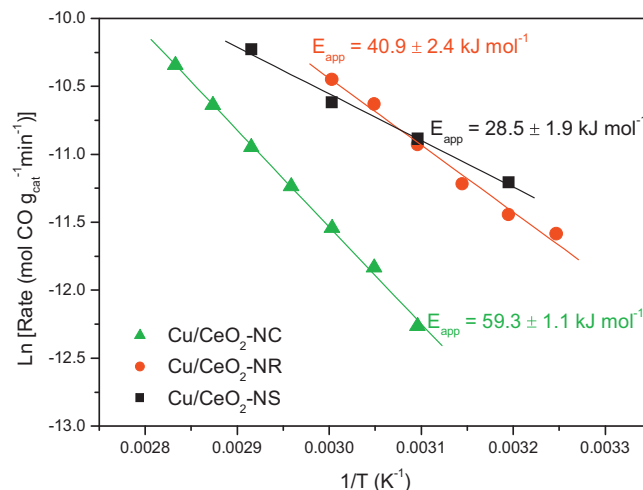

Fig. 9. Arrhenius plots for the CO oxidation reaction (under CO-PROX mixture) over the indicated catalysts.

oxygen on this surface, at ca. 530.5 eV, which can be ascribed to the presence of hydroxyl groups at the surface. By heating the sample in vacuum up to 200 °C in the main chamber, the evolved gases were mainly H_2O ($m/e = 18$) while the original shape of the O(1s) signals can be completely restored.

Comparing the XP spectra of the original catalysts pretreated in vacuum at 200 °C for 1 h the main difference observed was again the shape of the O(1s) signal in Cu/CeO_2-NC, similar to that found in the corresponding bare support, while the presence of the shake-up

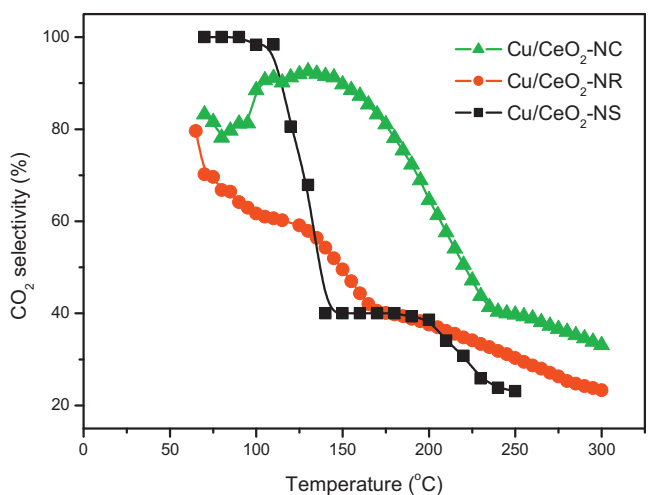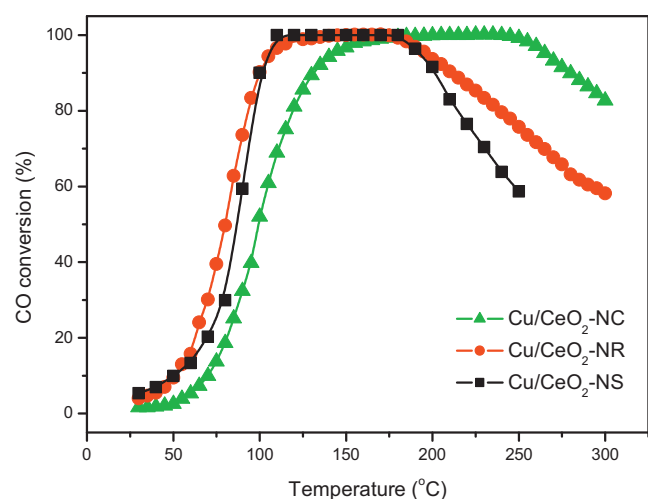**Fig. 8.** Catalytic activity under 1% CO, 1.25% O_2 and 50% H_2 (He balance) for the indicated catalysts. Top: CO conversion. Bottom: Selectivity to CO_2 among possible reactions of O_2 (see Experimental).

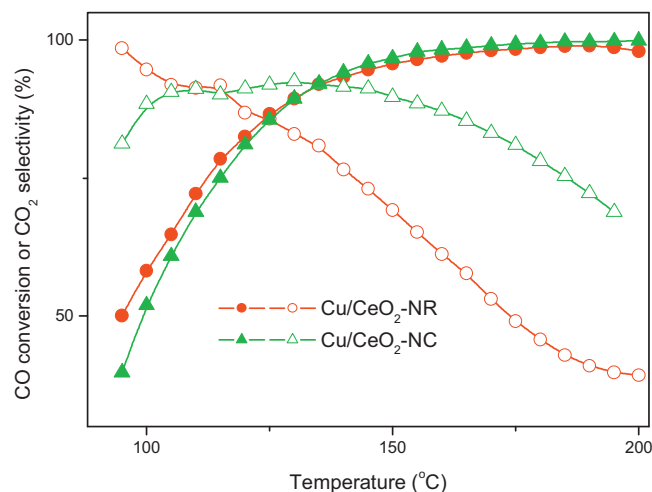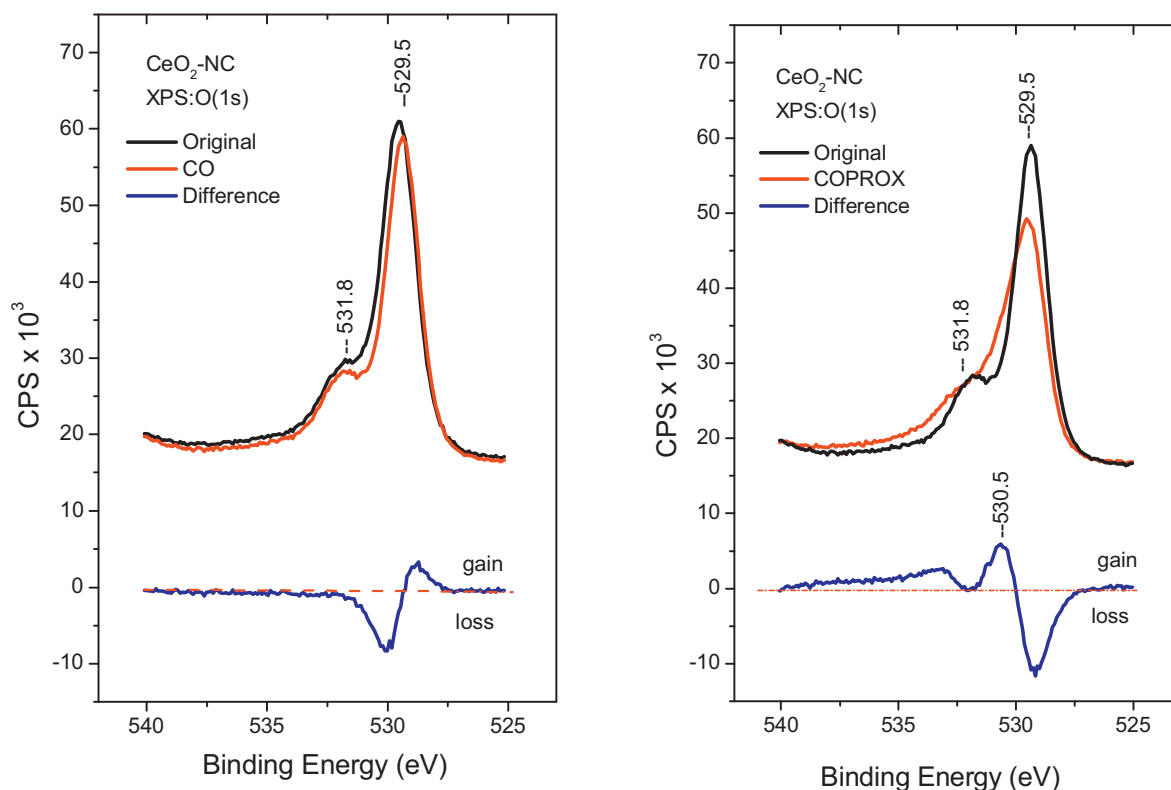**Fig. 10.** CO conversion (full symbols) and selectivity (open symbols) of Cu/CeO2-NC and Cu/CeO2-NR samples at matched contact times during tests with the catalytic reactor (using a GHSV of roughly 40,000 h^{-1} and 80,000 h^{-1} for the Cu/CeO$_2$-NC and Cu/CeO$_2$-NR catalysts, respectively).

Fig. 11. XPS spectra in the O(1s) region of CeO_2-NC subjected to indicated treatments (see Experimental part for details). Difference spectra are included (see main text).

satellites in the Cu(2p) signal indicates at least a partial oxidation of the copper to Cu^{2+} (see below). After reduction with CO at 200 °C some differences are observed in the spectra of all the catalysts. First, a higher level of reduction is observed in the Ce(3d) spectra (ca. 8% according to Factor Analysis of the results) and in the copper phase, which reaches a Cu_2O-like state (with a complete loss of the shake-up satellites in all the catalysts). Meanwhile, the O(1s) signal shows now similar shapes in all the reduced samples with the main peak at 529.7 eV and the smaller one at 531.9 eV now better defined and more symmetric also in samples Cu/CeO_2-NS and Cu/CeO_2-NR. Finally, in the region of C(1s), deposition of carbon species is observed at 285.6 eV and at 289.7 eV (overlapping with the intense Ce(4s) line at 289.9 eV) in the three samples, though in amounts which greatly depend on the type of catalyst: Cu/CeO_2-NS > > Cu/CeO_2-NR > Cu/CeO_2-NC. However, when the same pellets are subjected to stoichiometric CO/O_2 mixture at 200 °C, the peak at 285.6 eV was completely removed (except in Cu/CeO_2-NS where still ca. 40% remains) and the peak at 289.7 eV, showing contribution from carbonate species, also decreases as could be confirmed by subtracting the spectra. The Ce(3d) spectra indicate a complete reoxidation of the supports after such treatment under CO/O_2. CO-PROX conditioning of the catalysts (with CO:H_2:O_2 = 1:6:3 at 200 °C for 1 h) in similar way as carried out with the supports, while monitoring the gas phase evolution, shows CO_2 selectivities >95% for all three catalysts.

On the other hand, to examine in more detail the changes in the active Cu_xO phase after the different redox treatments, the energies of the $Cu(2p_{3/2})$ and $Cu(L_3M_{45}M_{45},{}^1G)$ peaks were plotted, together with the modified Auger parameter ($\alpha' = E_B + E_K$), in the form of Wagner-type chemical state diagrams, as shown in Fig. 12. According to Wagner [68], a shift in α' (shown as lines of "slope -1" in the diagrams) is related to differences in the extra-atomic relaxation energy ($\Delta\alpha' = 2\Delta R_{ea}$) according to a nonlocal core-hole screening relaxation mechanisms (final state effects). On the other

hand, within Moretti's electrostatic model [69], which assumes a nonlocal core-hole screening relaxation mechanism, lines with slope = −3 in these diagrams (two such lines being drawn in Fig. 12 passing through points marking the CuO and Cu_2O, bulk oxide references) correspond to species with the same chemical state (i.e. similar initial state effects).

Fig. 12 shows data for Cu/CeO_2-NS and Cu/CeO_2-NC obtained after the successive treatments labelled by numbers, including also, as references, data reported for bulk compounds or highly dispersed Cu_xO clusters in overloaded ZSM-5 zeolites [70]. Thus, for Cu/CeO_2-NS, the state of copper in the original sample outgassed at 200 °C was slightly more oxidized than after subsequent reduction with CO at 200 °C (points 1 and 2), the latter being closer to that of Cu_2O according to the corresponding dashed line of "slope -3"; nevertheless both points 1 and 2 have similar values of α' (slightly above that of the "slope -1" line for α' = 1848 eV) while the calculated Cu/(Cu + Ce) atomic ratio has decreased after the CO treatment from 11.8% to 8.6%. This may suggest a small growth of the Cu_xO particles which are now slightly more reduced but with a similar degree of interaction with the CeO_2-NS support ($\Delta\alpha' = \alpha_2' - \alpha_1' \approx 0$). However, when the catalyst is subsequently treated under stoichiometric CO/O_2 at 200 °C (point 3) its state is displaced toward the dashed line of "slope -3" of the CuO reference (i.e. it becomes more oxidised in correlation with the increase in the intensity of the satellite peak), while after the CO-PROX treatment (point 4) the copper phase becomes again more reduced. A final reduction with hydrogen at 200 °C (point 5) produces a fully reduced, dispersed Cu_2O-like copper phase. The small changes observed in the Cu/(Cu + Ce) atomic ratios after these treatments (9.4%, 10.9%, 11.2% for points 3, 4 and 5) suggest a great stability of the dispersed copper in the form of different (amorphous) copper oxides Cu_xO (1 < x < 2) dispersed on the surface of the support at each stage, probably with structures that can be described by successive insertion or loss of oxygen into the tetrahedral holes in
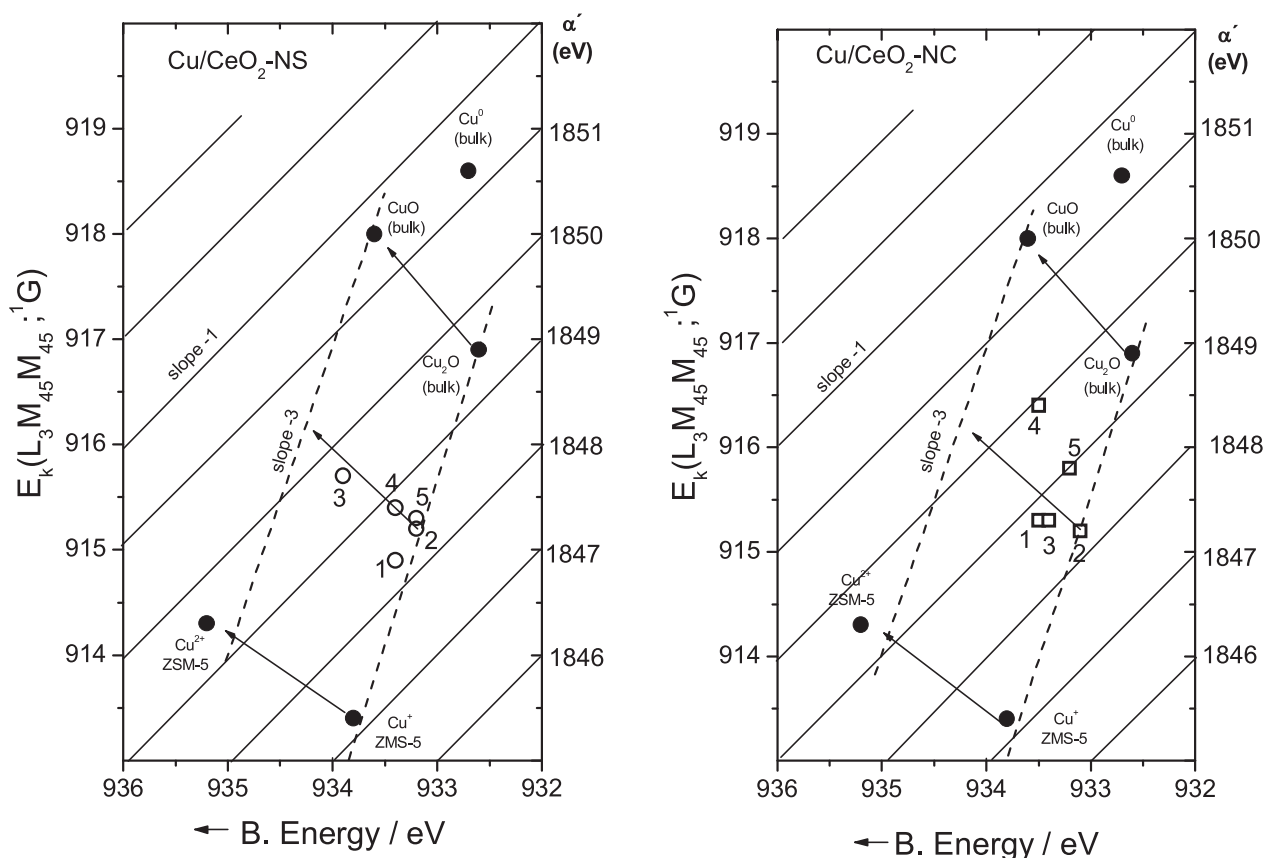
Fig. 12. Wagner diagrams (including lines with slope = −1 which correspond to constant values of Auger parameter α′ labelled at the right side) showing the evolution of Cu (2p and AES) XPS parameters during successive redox treatments performed in the specified order over the indicated catalysts. (1) Original outgassed at 200 °C; (2) reduction under CO at 200 °C; (3) Stoichiometric CO/O_2 mixture at 200 °C; (4) CO-PROX mixture at 200 °C; (5) H_2 at 200 °C.

the same network of (metallic) copper, in a similar manner as it is well known to occur between the stable copper oxide phases: Cu_2O, Cu_4O_3 and CuO [71–73].

Comparing these results with those found for the Cu/CeO$_2$-NC catalyst some differences are clearly observed (Fig. 12). First, in this case the copper in the original sample seems somewhat more oxidized, though it can be again almost completely reduced to a Cu_2O-like phase by CO at 200 °C (points 1 and 2). However, after treatment with stoichiometric CO/O_2 at 200 °C (point 3) it still remains mostly reduced, while after CO-PROX conditioning (point 4) the copper phase appears on the contrary significantly more oxidized; note also that the latter point is displaced upwards indicating a growth of the Cu$_x$O particles and/or changes in their interaction with the CeO$_2$-NC support, which modify the extraatomic relaxation process ($\Delta\alpha' = 2\Delta R_{ea}$). Values of the Cu/(Cu + Ce) atomic ratios for points 3 and 4 (14.7% and 16.5%, respectively, the latter being similar to that of the original sample) seems to discard the first option. Thus, a change in the interaction of the Cu$_x$O phase with the CeO$_2$-NC support, which favours a higher oxidation state of the copper in the presence of H_2 in the reactant mixture (under the CO-PROX conditions), has taken place and could be related to the incorporation of OH-groups to the CeO$_2$-NC support (Fig. 11). When the results for both catalysts, Cu/CeO$_2$-NS and Cu/CeO$_2$-NC, are compared, an apparently different behaviour is observed: in the Cu/CeO$_2$-NS catalyst, the copper, after stoichiometric CO/O_2 oxidation, remains more oxidized but it is easily reduced under the slightly reducing CO-PROX conditions used. In the Cu/CeO$_2$-NC catalyst, on the contrary, after treatment under stoichiometric CO/O_2 mixture, copper remains more reduced but it becomes more oxidized after CO-PROX conditioning. Since the main difference

between these two experiments (points 3 and 4 for both catalysts) is the absence or presence of H_2 it is worthy to compare the reduction of the copper by CO and by H_2 (points 2 and 5). While CO is able to reduce copper oxide close to a Cu_2O-like state in both catalysts, reduction by H_2 appears more complete for the Cu/CeO$_2$-NS catalysts. This can be also related to the existence of bigger Cu$_x$O particles in the Cu/CeO$_2$-NC catalyst which could explain the better CO_2 selectivity under CO-PROX conditions in this catalyst (see Fig. 7). Data for the Cu/CeO$_2$-NR catalysts (not shown) are initially quite similar to those the Cu/CeO$_2$-NC catalyst (points 1, 2 and 3), but after CO-PROX conditioning the Cu$_x$O phase appears now fully oxidized (as a CuO-like phase) while after hydrogen reduction it appears fully reduced to a Cu_2O-like phase. Cu/(Cu + Ce) atomic ratios again remain unchanged throughout all the experiments (original: 11.5%, CO-PROX: 11.0% and H_2: 11.1%).

In summary, the XPS data suggest that the more appropriate (from the selectivity point of view) combination of Cu$_x$O-active phase and CeO$_2$-support requires, under the CO-PROX conditions used, a stable moderate degree of oxidation of the Cu$_x$O phase (with $1 < x < 2$); this is probably favoured by the relatively big particle sizes of copper oxide entities in Cu/CeO$_2$-NC, which allows the presence of many Cu$^+$ sites in the more reducible boundaries of the copper particles in contact with the support (see below) where adsorption of CO occurs while it prevents direct reduction of the particles free surface (and bulk) where hydrogen could be oxidized, this is better achieved by the interaction of the Cu$_x$O phase with the CeO$_2$-NC support, which will favour an easy reduction at the boundary of the particles in contact with the support. This state is characterized by an Auger parameter of $\alpha' = 1850.0$ eV in the Cu/CeO$_2$-NC catalyst, between those for CuO and Cu_2O (1851.5 and 1849.5 eV),
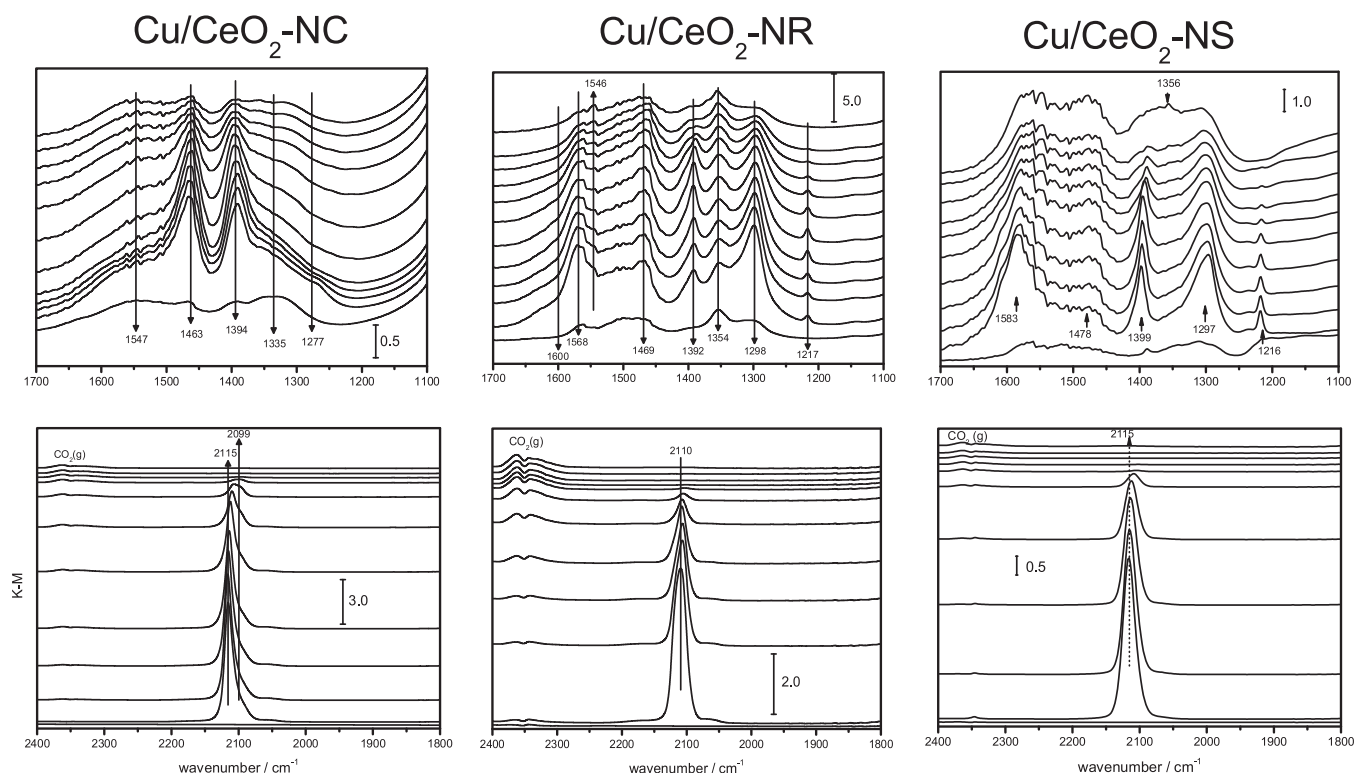
Fig. 13. DRIFT spectra for the indicated catalysts (left: Cu/CeO$_2$-NC; middle: Cu/CeO$_2$-NR; right: Cu/CeO$_2$-NS). The bottom spectrum in each case was recorded prior to introduction of the 1% CO + 1.25% O$_2$ + 50% H$_2$ mixture, and the rest were recorded in a stepped way (see Experimental) from 30 °C up, every 20 °C, under such CO-PROX mixture (from bottom to top).

which defines an appropriate level of reduction of the copper. In the Cu/CeO$_2$-NS and Cu/CeO$_2$-NR catalysts, with much smaller Cu$_x$O particles, a fine tuning of the above conditions appears more difficult. The much smaller Cu$_x$O-particles forming their active phases are now either easily fully oxidized or reduced or both, critically depending on the composition (and redox) characteristics of the gas phase, in spite of the stable interaction between the two phases (CeO$_2$ and Cu$_x$O) as indicated by the constant Cu/(Cu + Ce) atomic ratio values obtained also for these two catalysts. In any case, the XPS results demonstrate the higher difficulty for reduction by H$_2$ of copper oxide entities in Cu/CeO$_2$-NC. This, according to previous work [5], appears most relevant to maintain a relatively high degree of CO$_2$ selectivity in this sample.

3.2.2. Operando-DRIFTS study

Fig. 13 shows the DRIFT spectra observed under CO-PROX conditions for the three Cu-containing samples while relevant catalytic activity results obtained from corresponding on-line MS gas monitoring are shown in Fig. 14. Concerning these latter, as observed with the tubular catalytic reactor (Fig. 8), Cu/CeO$_2$-NS and Cu/CeO$_2$-NR show CO conversion profiles close to each other while Cu/CeO$_2$-NC clearly shows lower CO oxidation activity; this latter also differs from the two former in the fact that it displays the best characteristics in terms of CO$_2$ selectivity. It must be noted that differences between activity results obtained during the two experiments (Figs. 8 and 14) must be mainly attributed to differences in the type of reactors employed in each case [4].

Most strong changes observed in the DRIFT spectra in the presence of the reactant mixture are observed in the zones corresponding to carbonyl and carbonate species, as shown in Fig. 13; minor changes are also observed to be produced in the zone corresponding to hydroxyl species (not shown), taking place basically when water is produced as a consequence of H$_2$ oxidation, as

examined elsewhere [4]. Concerning evolution of carbonate species, different species are formed in the presence of the reactant mixture, in accordance with analysis of the 1700–1100 cm^{-1} region at which most intense bands for such species appear. Thus, bands at 1583–1548 and 1354–1271 cm^{-1} can be assigned to different types of bi- or tri-dentate carbonates [74,75]; the band at 1216 cm^{-1}, along with that at 1399 cm^{-1} and a shoulder at ca. 1600 cm^{-1}, are attributed to hydrogen carbonate species [4,74,75]. In turn, bands at 1469–1463 cm^{-1} and 1394–1392 cm^{-1}, whose formation appears most favoured for samples exposing (1 0 0) faces of ceria, can be attributed to mono- or tri-dentate carbonate species [74–77]. In turn, at relatively high reaction temperature, bands due to formate species appear, as evidenced by C–H stretching modes observed in the 2940–2830 zone (not shown), whose most intense C–O stretching modes appear at ca. 1585 and 1356 cm^{-1}. In any of the cases, the bands described corresponding to most intense ones observed in this zone (we cannot discard the presence of other more poorly defined or less intense overlapping bands) appear similar to those observed in the absence of copper (data not shown) and must therefore be attributed to species formed on ceria more or less affected by the presence of copper in the catalysts [75–77], in accordance also with independent CO oxidation experiments performed by DRIFTS over the corresponding Cu-free supports (not shown).

Bands observed in the 2115–2099 cm^{-1} region can be attributed to Cu$^+$-carbonyls, according to details reported elsewhere [4,74]. Two Cu$^+$-carbonyls yielding bands at ca. 2115 and 2099 cm^{-1}, this latter apparently more thermally stable, are detected for Cu/CeO$_2$-NC while somewhat wider single Cu$^+$-carbonyl bands at ca. 2110 and 2115 cm^{-1} are observed for Cu/CeO$_2$-NR and Cu/CeO$_2$-NS, respectively. Noteworthy, the intensity of Cu$^+$-carbonyls bands appears highest on Cu/CeO$_2$-NC (Fig. 15), despite the fact that this sample has the lowest specific surface and displays the lowest CO oxidation activity among the examined samples (Fig. 13). The
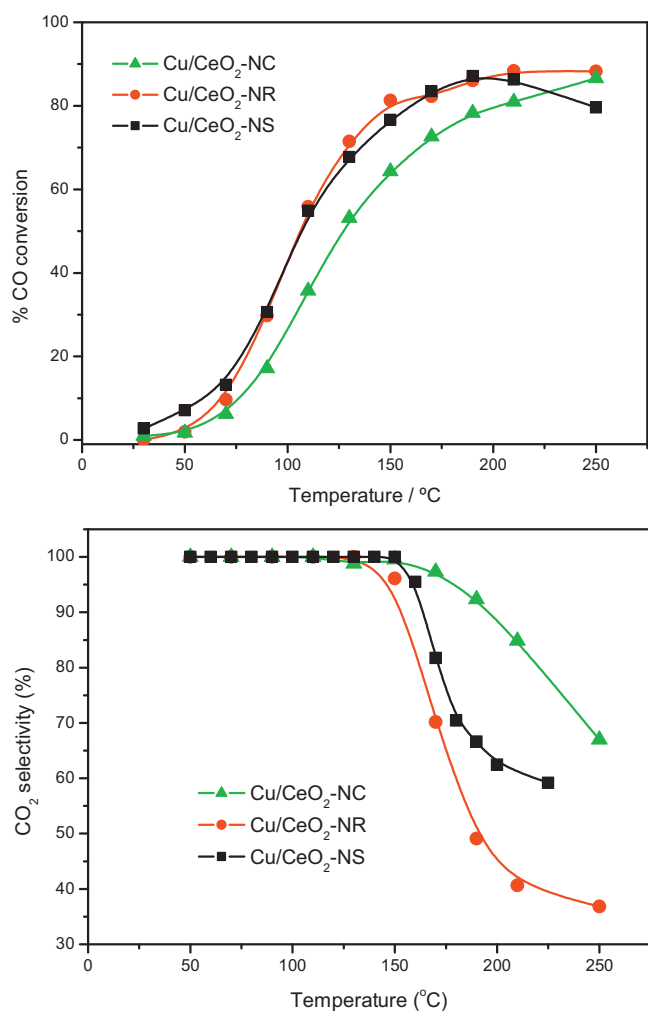
Fig. 14. Catalytic activity obtained during DRIFTS experiments shown in Fig. 12 under 1% CO, 1.25% O_2 and 50% H_2 (He balance) for the indicated catalysts. Top: CO conversion. Bottom: Selectivity to CO_2 among possible reactions of O_2 (see Experimental).
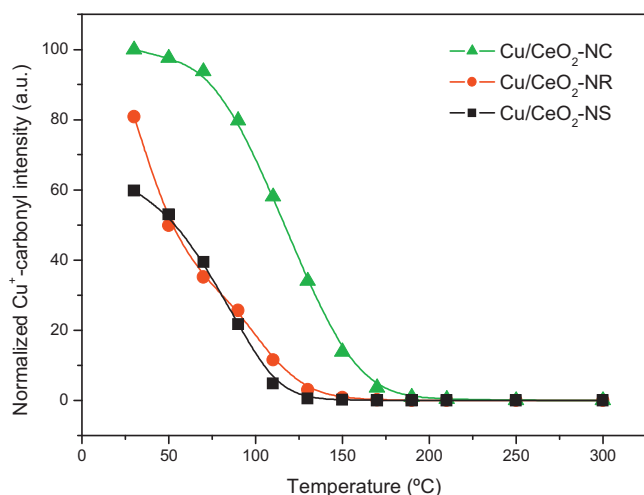
Fig. 15. Evolution of the intensity of the Cu^+ carbonyl band (see main text) during the DRIFTS experiments shown in Fig. 12.

absence of correlation between Cu^+-carbonyls intensity and CO oxidation rate appears here in contradiction with previous findings which demonstrated such connection within a set of samples prepared by the same microemulsion-based method (i.e. with similar ceria surface morphology) [4,5]. In principle, the intensity of Cu^+-carbonyls gives a measure of the amount of CO oxidation active sites formed at the interface upon reductive interaction with the CO-PROX mixture [4,5,17]. It therefore appears that active interfacial Cu^+ entities present different CO oxidation activity as a function of the CeO_2 face with which they interact, as in principle also supported by the differences in apparent activation energy exhibited in Fig. 9. Differences in the chemical behaviour of such Cu^+ entities is also pointed out by the different shift experienced by Cu^+-carbonyls frequency in each case. The presence of a stable Cu^+-carbonyl at 2099 cm^{-1}, strongly shifted to the red from that of the same type of carbonyls observed on Cu_2O (stable Cu^+-carbonyls formed on most energetically favoured monocoordinated sites appear at ca. 2125 cm^{-1} [78]), suggests a stronger degree of interaction with the support in Cu/CeO_2-NC, in agreement with the discussion above on the basis of characterization results. Such stronger interaction with the support can facilitate a higher relaxation and as a consequence a lower reactivity of the corresponding copper oxide species; DFT quantum modelling experiments are in course in this respect in order to attempt to demonstrate this hypothesis. Nevertheless, a positive consequence of such stronger Cu_xO-CeO_2 interaction seems to be a poorer H_2 oxidation activity leading to the appreciably higher CO_2 selectivity exhibited by Cu/CeO_2-NC, which allows observation of a wider maximum CO conversion window (Fig. 8), most interesting from a practical point of view. The reason for such lower H_2 oxidation activity over this sample could be the same one pointed out in the case of inverse CeO_2/CuO catalysts [7]. Such inverse configurations were shown to enhance CO-PROX properties with respect to direct CuO/CeO_2 systems, which was attributed to the higher difficulty for the deeper reduction of copper oxide (which provides the active sites for the H_2 oxidation reaction) upon increasing copper oxide particle size. In the case of Cu/CeO_2-NC, the strong interaction of copper oxide with the ceria support, facilitated by the specific (1 0 0) surfaces in it, can favour formation of non-segregated and, as a consequence of the low specific surface area, relatively larger copper oxide particles, according to characterization results summarized in the model exposed in Fig. 7. Such copper oxide particles appear in turn on their whole less reducible either due to its larger size or to interactions with the underlying support. Note in any case that it must be differentiated between reduction of copper oxide at interfacial positions (affecting to a relatively low amount of copper sites) and that of copper oxide at sites far from the interface and therefore less affected by interaction with the support. The former can be favoured in Cu/CeO_2-NC as a consequence of the interaction with the support and in view of achievement of highest Cu^+-carbonyls intensity under reaction conditions (Fig. 15), providing sites active for the CO oxidation reaction [5]. The latter will be most affected by the respective particle size and/or interaction with the support (discussion below) and would provide sites active for the H_2 oxidation reaction [5]. In any case, *operando*-DRIFTS results, as also supported by XPS results (Fig. 12), evidence the lower level of reduction achieved under CO-PROX conditions over Cu/CeO_2-NC since Cu^+-carbonyls show a slower decrease with increasing temperature than over the other two samples (Fig. 15). Note in this sense that previous redox experiments under CO over a catalyst similar to Cu/CeO_2-NS have shown such type of carbonyls to be stable up to at least ca. 250 °C [74]. Thus, the results in Fig. 15 point towards most favoured formation of metallic copper under CO-PROX conditions over Cu/CeO_2-NR and Cu/CeO_2-NS (Cu^+-carbonyl intensity practically vanishes at 150 and 130 °C, respectively, while still an appreciable concentration of CO(g) is present at those temperatures; note previous XANES

analysis demonstrated the evolution towards metallic copper upon increasing the temperature under CO-PROX mixture [5]), taking into account the poor thermal stability of metallic copper carbonyls which make them unobservable at such relatively high reaction temperature [74]. Such redox factor is therefore considered essential to maintain a higher selectivity level, taking into account that H_2 oxidation is most favoured upon increasing the reduction level in the copper component [2,5]. It may be noted in any case that with the here obtained data we cannot fully discard that such hindering of copper oxide reduction in Cu/CeO_2-NC, rather than being just a particle size effect, can be related to a specific effect of interaction with the (1 0 0) face of the support. Additionally, following arguments described in the Introduction, it may occur that differences in the copper oxide interaction with the support as a function of the exposed face in the latter modifies CO desorption characteristics (Fig. 15) within a reaction scheme in which CO and H_2 compete for the same active sites at relatively high reaction temperatures; reasons for the highest CO_2 selectivity observed for Cu/CeO_2-NC would in this case be determined by the highest stability of Cu^+-carbonyls in this latter. Further experiments would be required in order to confirm which of the hypotheses is most valid.

4. Conclusions

Three catalysts of 1 wt.% copper supported on ceria supports differing in their respective morphologies (nanocubes, nanorods and nanospheres or nanopolyhedra) have been prepared by copper impregnation on supports prepared by different methods (hydrothermal with varying synthesis parameters and microemulsion/precipitation). A model of structural characteristics of the catalysts has been established on the basis of a multitechnique (XRD, S_{BET} measurement, Raman, HREM, XPS, TPR and EPR) study. Copper appears mainly in the form of dispersed copper oxide entities at the surface of ceria in any of the catalysts although a stronger interaction with (1 0 0) surfaces present in ceria nanocubes is proposed which would favour the dispersion of copper oxide particles and modify their physicochemical properties. This is revealed by differences with respect to CO-PROX performance observed in each case. Thus, the sample supported on ceria nanocubes displays an enhanced CO_2 selectivity during the process which is attributed to the ability of such sample to keep a lower reduction level under reaction conditions. This could be related either to the relatively larger size of interacting dispersed copper oxide particles achievable, in part as a consequence of its lower specific surface area, in this sample and/or to effects of interaction with the (1 0 0) face present in the ceria support. The absence of correlation between CO oxidation activity and intensity of Cu^+-carbonyls formed under CO-PROX reaction conditions (as explored by *operando*-DRIFTS), which contrasts with previous results obtained with series of different copper loading samples supported on a ceria support with the same morphology or with samples prepared by copper-cerium microemulsion/coprecipitation [4,5], reveals differences in the catalytic properties of the dispersed copper oxide entities as a function of the surface characteristics of the ceria support with which they interact, i.e. a structural dependence of the CO-PROX reaction. On the whole, the main conclusion can be that optimized CO-PROX catalysts can be obtained by using ceria nanocubes as support. This is based on the fact that such morphology could allow achieving maximum dispersion (i.e. avoiding copper oxide segregation into separated big particles not interacting with the underlying support, as detected, for instance, when using ceria nanospheres as support [4]) and, in this case and partly as a consequence of its relatively low specific surface area, larger particle size within homogeneously distributed dispersed copper oxide particles; interaction of such dispersed copper oxide particles with the underlying (1 0 0) face of

ceria can also be most relevant to explain the enhanced CO-PROX catalytic properties. The latter is basically related to the enhanced CO_2 selectivity which favourably balances the decrease of CO oxidation activity produced as a consequence of the stronger interaction with the support. The higher CO_2 selectivity observed over the specimen supported on ceria nanocubes is shown to be related to difficulties to achieve full reduction of the dispersed copper oxide particles under CO-PROX conditions, on the basis of mainly *operando*-DRIFTS experiments.

Acknowledgements

References

[1] G. Avgouropoulos, T. Ioannides, C. Papadopoulou, J. Batista, S. Hocevar, H.K. Matralis, Catalysis Today 75 (2002) 157.
[2] K.-Y. Kim, J. Han, S.W. Nam, T.-H. Lim, H.-I. Lee, Catalysis Today 131 (2008) 431.
[3] A. Martínez-Arias, D. Gamarra, M. Fernández-García, A. Hornés, P. Bera, Zs. Koppány, Z. Schay, Catalysis Today 143 (2009) 211.
[4] D. Gamarra, G. Munuera, A.B. Hungría, M. Fernández-García, J.C. Conesa, P.A. Midgley, X.Q. Wang, J.C. Hanson, J.A. Rodríguez, A. Martínez-Arias., Journal of Physical Chemistry C 111 (2007) 11026.
[5] D. Gamarra, C. Belver, M. Fernández-García, A. Martínez-Arias., Journal of the American Chemical Society 129 (2007) 12064.
[6] H.C. Lee, D.H. Kim, Catalysis Today 132 (2008) 109.
[7] A. Hornés, A.B. Hungría, P. Bera, A. López Cámara, M. Fernández-García, A. Martínez-Arias, L. Barrio, M. Estrella, G. Zhou, J.J. Fonseca, J.C. Hanson, J.A. Rodriguez, Journal of the American Chemical Society 132 (2010) 34.
[8] A.-P. Jia, S.-Y. Jiang, J.-Q. Lu, M.-F. Luo, Journal of Physical Chemistry 114 (2010) 21605.
[9] A. Martínez-Arias, A.B. Hungría, M. Fernández-García, J.C. Conesa, G. Munuera, Journal of Physical Chemistry B 108 (2004) 17983.
[10] A. Martínez-Arias, A.B. Hungría, M. Fernández-García, J.C. Conesa, G. Munuera, Journal of Power Sources 151 (2005) 32.
[11] A. Martínez-Arias, M. Fernández-García, O. Gálvez, J.M. Coronado, J.A. Anderson, J.C. Conesa, J. Soria, G. Munuera, Journal of Catalysis 195 (2000) 207.
[12] A. Martínez-Arias, A.B. Hungría, M. Fernández-García, A. Iglesias-Juez, J. Soria, J.C. Conesa, J.A. Anderson, G. Munuera, Physical Chemistry Chemical Physics 14 (2012) 2144.
[13] E. Moretti, M. Lenarda, L. Storaro, A. Talon, R. Frattini, S. Polizzi, E. Rodríguez-Castellón, A. Jiménez-López., Applied Catalysis B 72 (2007) 149.
[14] A. Gurbani, J.L. Ayastuy, M.P. González-Marcos, M.A. Gutiérrez-Ortiz., International Journal of Hydrogen Energy 35 (2010) 11582.
[15] T. Caputo, L. Lisi, R. Pirone, G. Russo, Industrial and Engineering Chemistry Research 46 (2007) 6793.
[16] R. Kydd, D. Ferri, P. Hug, J. Scott, W.Y. Teoh, R. Amal, Journal of Catalysis 277 (2011) 64.
[17] C.S. Polster, H. Nair, C.D. Baertsch, Journal of Catalysis 266 (2009) 308.
[18] D. Gamarra, A. Martínez-Arias., Journal of Catalysis 263 (2009) 189.
[19] D. Gamarra, M. Fernández-García, C. Belver, A. Martínez-Arias., Journal of Physical Chemistry C 114 (2010) 18576.
[20] W. Liu, M. Flytzani-Stephanopoulos., Chemical Engineering Journal 64 (1996) 283.
[21] B. Skårman, L.R. Wallenberg, P.-O. Larsson, A. Andersson, J.-O. Bovin, S.N. Jacobsen, U. Helmersson, Journal of Catalysis 181 (1999) 6.
[22] K. Zhou, R. Xua, X. Sun, H. Chen, Q. Tian, D. Shen, Y. Li, Catalysis Letters 101 (2005) 169.
[23] L. Liu, Z. Yao, Y. Deng, F. Gao, B. Liu, L. Dong, ChemCatChem 3 (2011) 978.
[24] J. Han, H.J. Kim, S. Yoon, H. Lee, Journal of Molecular Catalysis A 335 (2011) 82.
[25] H.-X. Mai, L.-D. Sun, Y.-W. Zhang, R. Si, W. Feng, H.-P. Zhang, H.-C. Liu, C.-H. Yan, Journal of Physical Chemistry B 109 (2005) 24380.
[26] A. Martínez-Arias, M. Fernández-García, V. Ballesteros, L.N. Salamanca, J.C. Conesa, C. Otero, J. Soria, Langmuir 15 (1999) 4796.
[27] A. Hornés, P. Bera, M. Fernández-Garcia, A. Guerrero-Ruiz, A. Martínez-Arias, Applied Catalysis B 111–112 (2012) 96.
[28] V.D. Araujo, J.D.A. Bellido, M.I.B. Bernardi, J.M. Assaf, E.M. Assaf, International Journal of Hydrogen Energy 37 (2012) 5498.
[29] S.J. Tinnemans, M.H.F. Kox, M.W. Sletering, T.A. Nijhuis, T. Visser, B.M. Weckhuysen, Physical Chemistry Chemical Physics 8 (2006) 2413.
[30] F.C. Meunier, Chemical Society Reviews 39 (2010) 4602.
[31] http://srdata.nist.gov/xps/.

[32] F. Castellino, S.B. Rasmussen, A.D. Jensen, J.E. Johnsson, R.Fehrmann., Applied Catalysis B 83 (2008) 110.
[33] K.M. Eriksen, R. Fehrmann, N.J. Bjerrum, Journal of Catalysis 132 (1991) 263.
[34] X.Q. Wang, J.C. Hanson, J.A. Rodriguez, D. Gamarra, A. Martínez-Arias, M. Fernández-García., Journal of Physical Chemistry B 110 (2006) 428.
[35] S. Tsunekawa, K. Ishikawa, Z.-Q. Li, Y. Kawazoe, A. Kasuya, Physical Review Letters 85 (2000) 3440.
[36] X.-D. Zhou, W. Huebner, Applied Physics Letters 79 (2001) 3512.
[37] F. Zhang, S.-W. Chan, J.E. Spanier, E. Apak, Q. Jin, R.D. Robinson, I.P. Herman, Applied Physics Letters 80 (2002) 127.
[38] M. Fernández-García, A. Martínez-Arias, J.C. Hanson, J.A. Rodriguez, Chemical Reviews 104 (2004) 4063.
[39] X. Wang, J.A. Rodriguez, J.C. Hanson, D. Gamarra, A. Martínez-Arias, M. Fernández-García., Journal of Physical Chemistry B 109 (2005) 19595.
[40] M.-F. Luo, J.-M. Ma, J.-Q. Lu, Y.-P. Song, Y.-J. Wang, Journal of Catalysis 246 (2007) 52.
[41] B. Skårman, T. Nakayama, D. Grandjean, R.E. Benfield, E. Olsson, K. Niihara, L.R. Wallenberg, Chemistry of Materials 14 (2002) 3686.
[42] W.H. Weber, K.C. Hass, J.R. McBride., Physical Review B 48 (1993) 178.
[43] J.E. Spanier, R.D. Robinson, F. Zhang, S.-W. Chan, I.P. Herman, Physical Review B 64 (2001) 245407.
[44] J.R. McBride, K.C. Hass, B.D. Poindexter, W.H. Weber, Journal of Applied Physics 76 (1994) 2435.
[45] Z. Wu, M. Li, S.H. Overbury, Journal of Catalysis 285 (2012) 61.
[46] L. Mendelovici, H. Tzehoval, M. Steinberg, Applied Surface Science 17 (1983) 175.
[47] J.L.G. Fierro, J. Soria, J. Sanz, J.M. Rojo, Journal of Solid State Chemistry 66 (1987) 154.
[48] M. Figaj, K.D. Becker, Solid State Ionics 141–142 (2001) 507.
[49] A. Martínez-Arias, M. Fernández-García, J. Soria, J.C. Conesa, Journal of Catalysis 182 (1999) 367.
[50] F. Mehran, S.E. Barnes, G.V. Chandrashekhar, T.R. McGuire, M.W. Shafer, Solid State Communications 67 (1988) 1187.
[51] A. Abou Kaïs, A. Bennani, C.F. Aïssi, G. Wrobel, M. Guelton, J. Védrine, Journal of the Chemical Society, Faraday Transactions 88 (1992) 615.
[52] J. Soria, J.C. Conesa, A. Martínez-Arias, J.M. Coronado, Solid State Ionics 63–65 (1993) 755.
[53] M.-F. Luo, Y.-J. Zhong, X.-X. Yuan, X.-M. Zheng, Applied Catalysis A 162 (1997) 121.
[54] D. Gamarra, A. Hornés, Zs Koppány, Z. Schay, G. Munuera, J. Soria, A. Martínez-Arias., Journal of Power Sources 169 (2007) 110.
[55] T. Caputo, L. Lisi, R. Pirone, G. Russo, Applied Catalysis A 348 (2008) 42.
[56] A. Pintar, J. Batista, S. Hocevar, Journal of Colloid and Interface Science 285 (2005) 218.
[57] P. Zimmer, A. Tschope, R. Birringer, Journal of Catalysis 205 (2002) 339.
[58] X. Tang, B. Zhang, Y. Li, Y. Xu, Q. Xin, W. Shen, Applied Catalysis A 288 (2005) 116.
[59] J. Ciston, R. Si, J.A. Rodriguez, J.C. Hanson, A. Martínez-Arias, M. Fernández-García, Y. Zhu, Journal of Physical Chemistry C 115 (2011) 13851.
[60] J.C. Conesa, Surface Science 339 (1995) 337.
[61] Z. Yang, T.K. Woo, M. Baudin, K. Hermansson, Journal of Chemical Physics 120 (2004) 7741.
[62] S. Fabris, G. Vicario, G. Balducci, S. de Gironcoli, S. Baroni, Journal of Physical Chemistry B 109 (2005) 22860.
[63] L. Barrio, M. Estrella, G. Zhou, W. Wen, J.C. Hanson, A.B. Hungría, A. Hornés, M. Fernández-García, A. Martínez-Arias, J.A. Rodriguez, Journal of Physical Chemistry C 114 (2010) 3580.
[64] A. Martínez-Arias, A.B. Hungría, G. Munuera, D. Gamarra, Applied Catalysis B 65 (2006) 207.
[65] G. Sedmak, S. Hocevar, J. Levec, Journal of Catalysis 222 (2004) 87.
[66] A. Martínez-Arias, D. Gamarra, M. Fernández-García, A. Hornés, C. Belver, Topics in Catalysis 52 (2009) 1425.
[67] S. Lang, M. Türk, B. Kraushaar-Czarnetzki., Journal of Catalysis 286 (2012) 78.
[68] C.D. Wagner, Faraday Special Discussions of the Chemical Society 60 (1975) 291.
[69] G.J. Moretti, Electron Spectroscopy and Related Phenomena 95 (1998) 95.
[70] W. Grünert, N.W. Hayes, R.W. Joyner, E.S. Shpiro, M.R.H. Siddiqui, G.N. Baena, Journal of Physical Chemistry 98 (1994) 10832.
[71] M. O'Keeffe, B.G. Hyde, Structure and Bonding 61 (1985) 77.
[72] A. Vegas, Crystalline Reviews 7 (2000) 189.
[73] X. Wang, J.C. Hanson, A.I. Frenkel, J.-Y. Kim, J.A. Rodriguez, Journal of Physical Chemistry C 108 (2004) 13667.
[74] P. Bera, A. López Cámara, A. Hornés, A. Martínez-Arias., Journal of Physical Chemistry C 113 (2009) 10689.
[75] G.N. Vayssilov, M. Mihaylov, P.S. Petkov, K.I. Hadjiivanov, K.M. Neyman, Journal of Physical Chemistry C 115 (2011) 23435.
[76] C. Li, Y. Sakata, T. Arai, K. Domen, K. Maruya, T. Onishi, Journal of the Chemical Society, Faraday Transactions I 85 (1989) 929.
[77] C. Binet, M. Daturi, J.-C. Lavalley, Catalysis Today 50 (1999) 207.
[78] D. Scarano, S. Bordiga, C. Lamberti, G. Spoto, G. Ricchiardi, A. Zecchina, C. Otero Areán, Surface Science 411 (1998) 272.